
DELIVERABLE

D28.1 Report on methodologies for the real-time, automatic determination of fault geometry, source duration size parameters

Work package	WP28: Real-time earthquake shaking
Lead	Maren Böse, ETH Zurich
Authors	Maren Böse, ETH Zurich Simona Colombelli, UNINA Antonio Emolo, UNINA Sahar Nazeri, UNINA Stefania Tarantino, UNINA Simone Cesca, GFZ Nima Nooshiri, GFZ Alberto Michelini, INGV
Reviewers	Fabrice Cotton, GFZ
Approval	Management Board
Status	final
Dissemination level	public
Delivery deadline	31.10.2018
Submission date	31.10.2018
Intranet path	DOCUMENTS/DELIVERABLES



Table of Contents

Summary	3
1 Data.....	3
2 Algorithms	6
2.1 Event Detection & Rapid Line-Source Models.....	6
2.2 Rupture Dimensions, Moment Rate & Rapid Focal Mechanisms	6
2.3 Regional Moment Tensor & Rupture Directivity	8
2.4 Global Source Parameters	10
3 Results	10
3.1 Event Detection & Rapid Line-Source Models.....	10
3.2 Rupture Dimensions, Moment Rate & Rapid Focal Mechanisms	15
3.3 Regional Moment Tensor & Rupture Directivity	18
3.4 Global Source Parameters	22
3.4.1 Locations and Magnitudes.....	22
3.4.2 Focal Mechanisms.....	24
3.4.3 Tsunami Discriminant	25
4 Conclusions.....	26
5 References.....	29
Contact.....	32

Summary

Finite-source models of moderate and large earthquakes provide crucial information in potentially harmful events, if provided within seconds to minutes from event origin. Here we use the example of the 2016-2017 Central Italy earthquake sequence and a dataset of 19 large global earthquakes to demonstrate and compare the performance of four independent algorithms in the calculation of rapid finite-fault models.

1 Data

The Central Apennines are among the regions with the highest seismic hazard in Italy. They have an exceedance probability of 10% of the horizontal peak ground acceleration (PGA) value of 0.250 to 0.275 g in 50 years (Stucchi *et al.*, 2011). Several partially damaging earthquake sequences in the Central Apennines have been documented, including the 2016-2017 sequence with hundreds of earthquakes, including 13 normal fault M4.7+ earthquakes from which the three largest mainshocks (2016 Mw6.0 Amatrice, Mw5.9 Visso, and Mw6.5 Norcia) caused significant damage and fatalities. The sequence is still persistent and has so far activated a more than 60-km-long normal-fault system with a N150°E ($\pm 10^\circ$) striking plane and a series of 50° ($\pm 5^\circ$) southwest-dipping fault segments (Chiaraluce *et al.*, 2017).

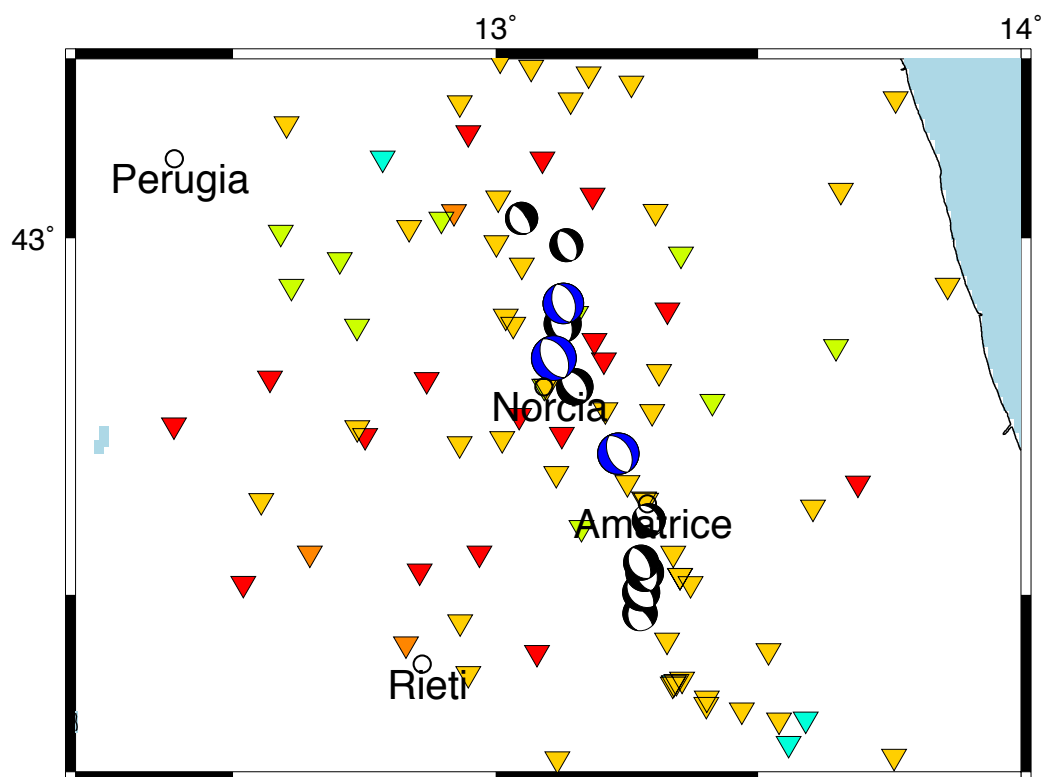


Figure 1.1. Our dataset comprises the 13 largest normal fault earthquakes ($4.7 \leq M_w \leq 6.5$) of the 2016-2017 Central Italy earthquake sequence, including the 2016 Mw6.0 Amatrice, Mw5.9 Visso, and Mw6.5 Norcia earthquakes. Most strong-motion stations (inverted triangles) of the “Rete Sismica Nazionale” (RSN) and “Rete Accelerometrica Nazionale” (RAN) Strong-Motion Networks operated by INGV and the Dipartimento della Protezione Civile (DPC), are deployed on class A (red) or B (yellow) sites according to the EC8 site classification, corresponding to rock and stiff soil, for which little site effects are expected.

For this study, we select a dataset of the 13 largest normal fault earthquakes ($4.7 \leq M_w \leq 6.5$) that occurred between January 2016 and December 2017 in the Central Apennines (latitude: 42.2° to 43.2° , longitude: 12.4° to 14.08°) (**Table 1.1** & **Figure 1.1**). We use the *Istituto Nazionale di Geofisica e Vulcanologia* (INGV) earthquake catalogue and finite-fault models of the three mainshocks by Tinti *et al.* (2016), Chiaraluce *et al.* (2017) and Scognamiglio *et al.* (2018) for reference. We collect local strong-motion waveforms recorded by the *Rete Sismica Nazionale* (RSN) and *Rete Accelerometrica Nazionale* (RAN) Strong-Motion Networks operated by INGV and the *Dipartimento della Protezione Civile* (DPC), as well as regional and global broadband waveforms recorded by various agencies.

Table 1.1. Source parameters of earthquakes in the 2016-2017 Central Italy sequence studied in this report.

REGION EVENT ID	DATE TIME (UTC)	LAT [$^\circ$]	LON [$^\circ$]	Z [KM]	ML	MW	STRIKE/DIP/RAKE [$^\circ$]
A./AMATRICE 7073641	2016-08-24 01:36:32.00	42.6983	13.2335	8.1	6.0	6.0	155/49/-87
NORCIA 7076161	2016-08-24 02:33:28.89	42.7922	13.1507	8.0	5.4	5.3	135/47/-98
AMATRICE 7224451	2016-08-26 04:28:25.91	42.6048	13.2915	8.7	4.7	4.8	128/53/-106
C.S. ANGELO 8663031	2016-10-26 17:10:36.34	42.8802	13.1275	8.7	5.4	5.4	161/38/-90
USSITA/VISSO 8669321	2016-10-26 19:18:05.85	42.9087	13.1288	7.5	5.9	5.9	159/47/-93
NORCIA 8863681	2016-10-30 06:40:17.36	42.8322	13.1107	9.2	6.1	6.5	151/47/-89
ACQUACANINA 9033461	2016-11-01 07:56:40.34	42.9902	13.1345	8.3	4.7	4.8	161/46/-82
ACQUACANINA 9166761	2016-11-03 00:35:01.29	43.0277	13.0493	8.1	4.7	4.7	162/24/-76
AMATRICE 12695491	2017-01-18 09:25:40.39	42.545	13.2768	10.0	5.3	5.1	153/32/-88
AMATRICE 12697591	2017-01-18 10:14:09.90	42.531	13.2838	9.6	5.4	5.5	161/51/-86
CAPITIGNANO 12697641	2017-01-18 10:15:33.40	42.5277	13.2852	8.8	4.7	-	unknown
AMATRICE 12698071	2017-01-18 10:25:23.73	42.5033	13.277	9.4	5.3	5.4	140/35/-89
MONTEREALE 12707401	2017-01-18 13:33:36.74	42.4733	13.2747	9.5	5.1	5.0	188/30/-39

We retrieve the quality-assured strong-motion waveforms for the 2016-2017 Central Italy earthquake sequence from the *Engineering Strong Motion* (ESM) database (<http://orfeus-eu.org/esm>; Luzi *et al.*, 2016). The broadband waveforms are downloaded via FDSN and EIDA webservices (<https://www.orfeus-eu.org/data/eida/webservices/>). These data require manual or automated interaction for quality assurance (**Chapter 3.3**).

Since one of the algorithms tested in this study (Early-Est, **Chapter 2.4**) provides source parameters for earthquakes at teleseismic distances, we additionally select a set of 19 global earthquakes with $M \geq 6.6$ that occurred between January 2017 and January 2018 (**Table 1.2** and **Figure 1.2**). For these earthquakes, we compare in this study the solutions produced by Early-Est with the Global Centroid Moment Tensor catalogue (Dziewonski *et al.*, 1981; Ekström *et al.*, 2012) available at

<http://www.globalcmt.org>). For the three mainshocks in the Central Italy sequence, we use the NEIC w-phase moment tensor solutions (mww) for reference, because the API used to download the data (obspyDMT, <https://github.com/kasra-hosseini/obspyDMT>) was not found to cover the time period before January 2017.

Table 1.2. Earthquakes used for testing of the Early-Est software, including the three largest events in the 2016-2017 Central Italy earthquake sequence and 19 additional global earthquakes with $M_{GCMT} \geq 6.6$.

event_id	datetime	latitude	longitude	depth	magnitude	magnitude_type	Mwp	Mwpa	region
20180225_174508.a	2018-02-25T17:45:08.600000Z	-6.29	142.97	12	7.5	Mwc	7.3	7.6	New Guinea, Papua New Guinea
20180216_233946.a	2018-02-16T23:39:46.300000Z	16.53	-97.88	20	7.2	Mwc	7.3	7.4	Oaxaca, Mexico
20180123_093204.a	2018-01-23T09:32:04.000000Z	56.22	-149.12	33.6	7.9	Mwc	7.5	7.6	Gulf of Alaska
20180114_091852.a	2018-01-14T09:18:52.300000Z	-15.95	-74.78	40.9	7.1	Mwc	7.0	7.1	Near Coast of Peru
20180110_025144.a	2018-01-10T02:51:44.300000Z	17.56	-83.86	16.5	7.5	Mwc	7.5	7.6	North of Honduras
20171113_022829.a	2017-11-13T02:28:29.400000Z	9.45	-84.58	29.6	6.6	Mwc	6.7	6.7	Costa Rica
20171112_181825.a	2017-11-12T18:18:25.300000Z	34.83	45.84	17.9	7.4	Mwc	7.1	7.3	Iran - Iraq Border Region
20171104_090031.a	2017-11-04T09:00:31.300000Z	-15.06	-173.09	35	6.7	Mwc	6.7	6.8	Tonga Islands
20171031_004221.a	2017-10-31T00:42:21.200000Z	-21.61	169.14	12.6	6.7	Mwc	6.6	6.8	Southeast of Loyalty Islands
20171024_104750.a	2017-10-24T10:47:50.300000Z	-7.25	123.02	556.8	6.7	Mwc	6.4	6.6	Banda Sea
20171010_185341.a	2017-10-10T18:53:41.300000Z	-53.89	8.92	16.4	6.7	Mwc	6.4	6.6	Bouvet Island Region
20170908_044946.a	2017-09-08T04:49:46.700000Z	15.38	-94.66	44.8	8.2	Mwc	7.9	8.0	Near Coast of Chiapas, Mexico
20170818_025939.a	2017-08-18T02:59:39.100000Z	-0.87	-14.15	22.2	6.6	Mwc	6.5	6.6	North of Ascension Island
20170720_223116.a	2017-07-20T22:31:16.400000Z	36.79	27.56	12	6.6	Mwc	6.7	6.9	Turkey
20170717_233451.a	2017-07-17T23:34:57.700000Z	54.13	169.78	23.2	7.8	Mwc	7.3	7.6	Komandorskiye Ostrova Region
20170622_123109.a	2017-06-22T12:31:09.100000Z	13.57	-91.38	38.1	6.8	Mwc	6.8	6.9	Near Coast of Guatemala
20170614_072907.a	2017-06-14T07:29:07.900000Z	14.92	-92.17	72.7	7.0	Mwc	6.8	6.8	Guatemala
20170602_222454.a	2017-06-02T22:24:54.100000Z	54.14	170.83	13.1	6.7	Mwc	6.6	6.7	Near Islands, Aleutian Islands
20170509_135215.a	2017-05-09T13:52:15.100000Z	-14.55	167.2	181.4	6.8	Mwc	6.6	6.6	Vanuatu Islands
20160824_013632.a	2016-08-24T01:36:32.870000Z	42.723	13.1877	4.44	6.2	mww	6.2	6.2	Central Italy
20161026_191808.a	2016-10-26T19:18:08.430000Z	42.9564	13.0666	10	6.1	mww	6.2	6.2	Central Italy
20161030_064018.a	2016-10-30T06:40:18.670000Z	42.8621	13.0961	8	6.6	mww	6.7	6.8	Central Italy

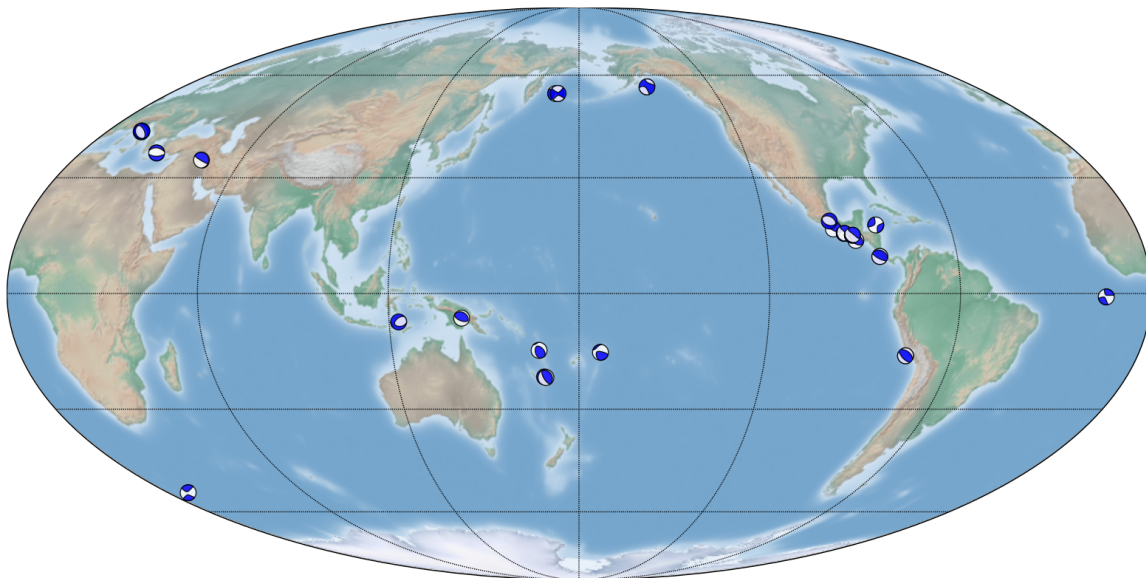


Figure 1.2. Locations of the 22 earthquakes used for testing of the Early-Est software.

2 Algorithms

In the following subchapters, we summarize each algorithm and provide relevant references.

2.1 Event Detection & Rapid Line-Source Models

The Finite-Fault Rupture Detector (FinDer) algorithm was originally proposed by Böse *et al.* (2012) to determine fast and robust line-source models of large earthquakes in order to enhance ground-motion predictions for earthquake early warning (EEW). Later, the algorithm was refined to quantify the uncertainties in the output models in terms of likelihood functions (Böse *et al.*, 2015) and to allow for an application across the magnitude range from M2 to M9 (Böse *et al.*, 2018).

The FinDer algorithm is based on template matching, in which the spatial distribution of high-frequency ground-motion amplitudes in a seismic network is continuously monitored and correlated with theoretical template maps. These templates are pre-computed from empirical ground-motion prediction equations (GMPEs) for line-sources of different lengths and magnitudes. The ground-motion amplitudes in these templates are distributed symmetrically around the line-source and decrease with increasing distance, as described by the GMPEs. The templates are rotated in order to constrain the strike of the earthquake fault rupture.

The template with the highest correlation with the observed ground-motion pattern is determined from a combined grid-search and divide-and-conquer approach (Böse *et al.*, 2018). The resulting model is characterized by the line-source centroid, length, strike and corresponding likelihood functions. The model is updated every second until peak shaking is reached, thus allowing fault ruptures to be mapped as they develop.

In previous studies (Böse *et al.*, 2012; Böse *et al.*, 2015; Böse *et al.*, 2018), we characterized the ground-motion patterns by the spatial distribution of peak ground acceleration (PGA) amplitudes, motivated by the observation that these high-frequency motions are mainly controlled by the distance to the fault rupture and that these motions are less affected by rupture directivity compared to long- and mid-period motions (e.g., Spudich and Chiou, 2008). Since the spatial dimensions of the templates usually cover tens to hundreds of kilometres in length and width, and thus large areas with different site conditions are considered simultaneously, Böse *et al.* (2018) argued that site corrections of the observed ground-motion amplitudes are unlikely to significantly affect the output model.

However, no systematic analysis of different ground-motion metrics and site corrections has been performed so far. To close this gap, in this study we compare the performance of FinDer for four template sets generated with GMPEs after Bindi *et al.* (2011), including templates produced for peak ground acceleration (PGA) and peak ground velocity (PGV), each with and without site corrections.

2.2 Rupture Dimensions, Moment Rate & Rapid Focal Mechanisms

Our second set of algorithms has the goal to provide straightforward and robust methodologies both for the rapid determination of the event size, as well as for a realistic characterization of the extended source in real-time. In particular, we use the initial P-wave peak displacement, velocity and acceleration amplitudes to constrain the possible geometry of the fault plane (in terms of size and spatial orientation) in real-time. Our activities are two-fold:

Activity 1 – Real-Time Characterization of the Extended Seismic Source: In this activity, we analyse how the initial P-wave signals are suited for the rapid characterization of the extended source. In particular, the time evolution of peak amplitude parameters is used for the rapid prediction

of the source magnitude and extent, as well as for estimating and modelling of the moment rate function.

Following the methodology introduced by Colombelli and Zollo (2015), our approach is based on the progressive measurement of the P-wave maximum displacement amplitude (P_d) along the recorded seismograms, between the arrival of the P-wave and up to the arrival of the S-wave (**Figure 2.2.1b**). For each seismic event, a single curve is built (named *Logarithm of P-wave Time Window* curve, hereinafter LPDT), by averaging P_d at different recording stations, distributed over azimuth and distance. The basic assumption of our approach is that the LPDT curve is a proxy for the Moment Rate Function (MRF), which is the most reliable representation of the rupture process. Assuming a triangle-like MRF, the maximum level of the LPDT curve (T_{peak}) is reached at the peak of the MRF (**Figure 2.2.1a**).

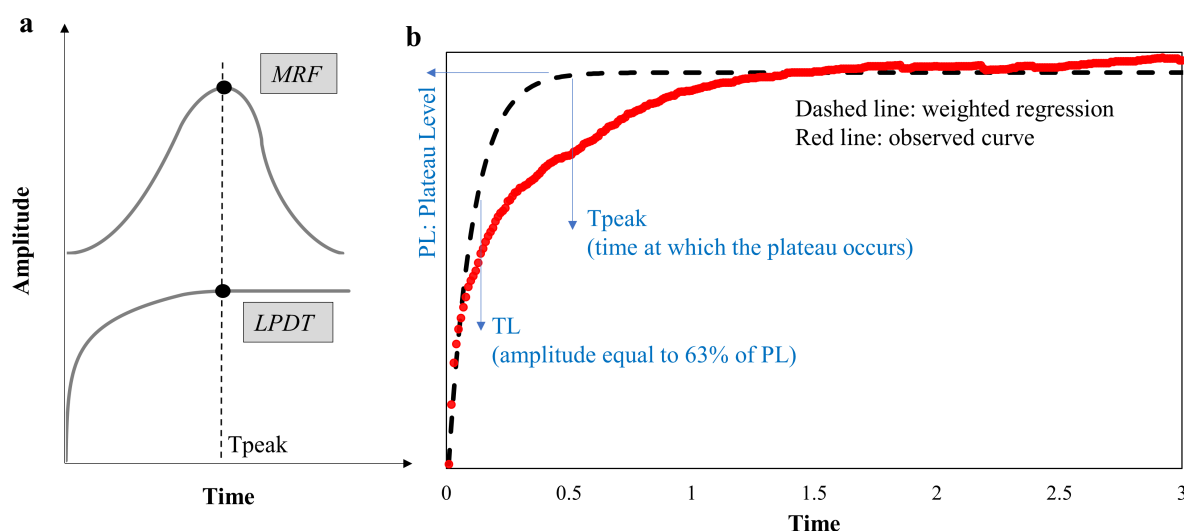


Figure 2.2.1. a) Schematic relationship between LPDT curves and MRF. b) Definition of the fitting parameters.

To model the observed curves, we use an exponential fitting function of the type:

$$y = P_L(1 - e^{-\frac{t}{T_L}}) + y_0$$

where P_L and T_L are to be estimated from the fitting procedure, and y_0 (which is the intercept of the curve) is fixed to the first point of the curve. To correctly estimate P_L and T_L , we apply a weighted regression procedure to fit the LPDT curve. T_{peak} is estimated from the fitted curves as the time at which the plateau occurs, and is used as a proxy for the half-duration of the MRF. The plateau level of the LPDT curves carries information on the maximum amplitude of the MRF. The corresponding saturation time is related to the half-width of the triangular function, so that the P_L and T_L parameters can be jointly used as proxies for the event magnitude and source duration, respectively, and, under the assumption of a constant rupture velocity, for the rupture dimensions. Finally, the available estimates of moment magnitude and source extension (radius) allow to determine the static stress drop, using the Keilis-Borok (1959) formula.

Activity 2 – Real-Time Fault-Plane Solution: This activity is dedicated to the real-time determination of the fault focal mechanism using the azimuthal distribution of P-wave displacement amplitudes and *a priori* constraints based, e.g., on the local tectonic information.

Input data for Activity 2 are the initial P-wave peak amplitudes, which are measured as the maximum absolute amplitude values of displacement, velocity and acceleration (Pd, Pv and Pa), respectively. These three parameters are estimated on the vertical component of the ground motion, in progressively expanding P-wave time windows, starting at the arrival of the P-wave. For a single earthquake, the peak amplitude parameters decrease as a function of distance. To account for the path effect, we correct the observed data for the distance using pre-computed empirical scaling relationships (relating the observed amplitude to earthquake magnitude and distance) and project the observed amplitudes onto the direction of the P-wave incidence (which requires the earthquake source location to be known). We then normalize the observed P-wave peak parameters to their maximum value (Pd, Pv and Pa are independently normalized) and combine them by computing the average, giving equal weight to each of the three amplitude parameters.

As soon as a few seconds of P-wave signals are available at a set of recording stations, the observed P-wave amplitude distribution is compared to the theoretical P-wave amplitude radiation pattern (as absolute value), for a set of potential fault geometries. The comparison is done through a dedicated octree algorithm (Fang *et al.*, 1996), and provides a first-order identification of the best solution for the fault mechanism. We developed a Bayesian, evolutionary approach, where the solution at each time step is used as *a priori* information for later times. To start the first iteration, we can either use an uninformative *prior* PDF or include tectonic information (or information from another algorithm, see **Chapter 4**) through a *prior* PDF of a specific shape. For example, we can choose a simple *prior* PDF (for strike, dip and slip) that is a given value within the desired range and that is ten times smaller outside of it. At each iteration, the convergence of the solution is evaluated by comparing the current solution at time i (m^i) with the most likely triplet of the previous step (m^{i-1}). Specifically, we evaluate the condition

$$\frac{\|m^{i-1} - m^i\|}{\|m^{i-1}\|} \leq \varepsilon$$

where $m = [strike, dip, slip]$ and $\varepsilon = 0.05$. The convergence is declared, if the previous condition is continuously satisfied for a 3 s-wide time window. The final solution is then obtained as a *posterior* PDF, and is characterized by its mean, mode and median values. The uncertainty on each parameter is also provided and is computed as the 68% confidence ellipsoid's projections centred on the best solution, from the *posterior*, marginal probability distribution for strike, dip and slip, separately.

The misfit of the solution is computed as

$$Misfit = \sum_j^{N_s} (R_j^d - |R_j^{th}|)^2$$

where $N_s(i)$ is number of available stations at time i , R_j^d is the observed absolute amplitude at station j , R_j^{th} is the absolute theoretical amplitude of P-wave at station j for model m^i .

The methodology described here is able to provide a quick and simple estimation of the focal mechanism that can be used to improve the existing approaches for Earthquake Early Warning (EEW) and rapid response without using polarities or waveform inversions.

2.3 Regional Moment Tensor & Rupture Directivity

The adopted regional moment tensor inversion algorithm was originally proposed by Cesca *et al.* (2010) and tested for a range of moderate to large tectonic earthquakes, under a double couple (DC) source approximation. The algorithm was later extended to a broader target of seismic signals, including those produced by induced seismicity, mining collapses, explosions and volcanic sources,

accounting for a full moment tensor (MT) representation (Cesca *et al.*, 2013). The original implementation in Cesca *et al.* (2010) fits full waveform amplitude spectra and displacement traces to resolve earthquake source parameters, namely centroid time, centroid location, strike, dip and rake angles for fault and auxiliary planes, scalar moment and moment magnitude, under a point source approximation. The amplitude spectra inversion is chosen as less sensitive to trace misalignment and velocity model inaccuracies (Domingues *et al.*, 2013), and it is accompanied by a time domain inversion to resolve the MT polarity. The procedure follows a multi-step inversion approach, where source parameters are not simultaneously resolved, but obtained in subsequent steps, fitting either full waveforms or their amplitude spectra at different frequency ranges. Following such philosophy, once source parameters are resolved for a point source approximation by fitting low frequency data, finite source parameters such as rupture size and duration could be inverted in a later step including higher frequency. This part of the inversion is, however, more time consuming, since it requires the simulation of synthetic seismograms for several extended source models with different geometries and sizes.

A quicker and simpler approach to derive some general source parameters describing the rupture kinematics was proposed by Cesca *et al.* (2011) and has been used in this project. The main idea is to detect azimuthal patterns of apparent source durations, which can be modelled by uni- or bilateral rupture processes. Technically, the approach requires the prior determination of point source parameters, either through regional moment tensor inversion or using the other techniques tested in the project. These analyses will constrain the focal mechanism, scalar moment and centroid depth. In the next iteration, we consider separately each station and derive first the apparent scalar moment by linear inversion, and then the apparent rupture duration by a grid search over a range of possible rupture durations. The resulting apparent duration describes the duration of the earthquake rupture as observed at that station. The azimuthal distribution of apparent durations can be modelled by a constant average duration and by theoretical curves for unilateral and bilateral ruptures with different directions, constrained on the base of the fault-plane orientations. For pure unilateral ruptures, for example, the azimuthal distribution of apparent durations can be well approximated by a cosine curve, with shorter apparent duration in the direction of rupture propagation. The distribution of apparent duration can be used to infer other source parameters, such as the rupture direction, the absolute rupture duration, the rupture length and, in some cases, the true fault-plane orientation. As a final step, an F-test can be used to judge the fit of apparent durations for competing rupture models characterized by different degrees of freedom, in order to automatically detect cases, where a uni- or bi-lateral rupture model is robustly resolved.

The combination of moment tensor and directivity analysis, triggered by the recognition of the earthquake occurrence and the provision of first source parameters (origin time, location, rough magnitude, and possibly a preliminary focal mechanism) from other fast near early-warning routines is performed over different subsequent steps: data and metadata acquisition, data quality control, moment tensor inversion, and directivity inversion. For automated implementation an important step concerns the data quality control, which can be automatized by using preliminary source parameters (location, magnitude, focal mechanism) to generate synthetic data, compare them to observations and identify problematic stations.

Previous applications of the moment tensor inversion tool include applications to regional seismicity (Domingues *et al.*, 2013), seismic sequences at subduction margins (Cesca *et al.*, 2016), induced seismicity (Cesca *et al.*, 2014; Grigoli *et al.*, 2018), seismic sources in volcanic environments (Del Fresno *et al.*, 2015) and nuclear explosions (Cesca *et al.*, 2017), while the rapid directivity inversion approach has been successfully used in Cesca *et al.* (2011, 2013) and Custodio *et al.* (2012) for different case studies.

2.4 Global Source Parameters

To determine additional global source parameters, we use in this study the software platform Early-Est (EE, <http://early-est.rm.ingv.it>), which has been designed for the rapid determination of location, magnitude, source-time duration, tsunami discriminants and fault-plane solutions. EE is adopted by the INGV-CAT Tsunami Service Provider for earthquake monitoring and tsunami alert in the area of competence in the Euro-Mediterranean region and for monitoring at global scale. The location procedure is based on a continuous identification of phases and on identifying the most appropriate location of earthquakes based on stacking of phase arrival times. This is done automatically at a predefined chosen time interval (1 minute timestamps). The software includes automatic calculations of magnitude (mb, Mwp and Mwpd) and of rupture duration from P-wave high frequencies.

The program *fmamp* is a prototype, probabilistic, global-search (oct-tree grid-search; Lomax *et al.*, 2009), mechanism determination code that uses first-motions and relative P amplitudes. The *fmamp* program determines mechanisms based on either first-motion polarities (*fmamp polarity*), high-frequency average P amplitude (*fmamp amp aref*, using the existing EE “aref” amplitude measure), or displacement amplitudes derived from the existing Mwp magnitude estimation in EE (*fmamp amp Mwp*). The sign of the amplitude measures is set from the measured first-motion polarities, recalling that a waveform polarity based on the Mwp measure is used when available in EE (Lomax and Michelini, 2012). Predicted radiation amplitudes are calculated using Aki and Richards (1980), eqs. 4.84 to 4.86.

For determination using polarities, the *fmamp* misfit function is based on a count of agreement between observed and predicted first-motion polarities for each tested fault-plane solution. This misfit function is similar to that used by other first-motion polarity focal mechanism inversion codes, such as HASH (Hardebeck and Shearer, 2002, 2003) or FPFIT (Reasenber and Oppenheimer, 1985).

Another parameter of interest, especially for tsunamigenic events, is the high frequency P-wave train duration (T_0), which by its nature contains information about the source extent and is used for the fast determination of large magnitude events (e.g., calculation of Mwpd, Lomax and Michelini, 2012; LM2012 hereinafter). T_0 is generally quite large for tsunami earthquakes – a particular type of earthquakes that regardless of the relatively small magnitude produce large tsunami – reflecting very shallow and long ruptures. LM2012 have shown that the TdT50Ex function calculated on-the-fly on the incoming earthquake waveforms is an effective discriminant of earthquakes, which are potentially tsunamigenic. The TdT50Ex discriminant function combines the dominant period of the incoming P-waves with the high-frequency duration.

3 Results

In the following subchapters, we summarize the performance of each algorithm for the 13 test events in the 2016-2017 Central Italy earthquake sequence (**Table 1.1**), and – in the case of the Early-Est software – for an additional set of 19 global earthquakes that occurred in 2017 and 2018 (**Table 1.2**).

3.1 Event Detection & Rapid Line-Source Models

In this study, we test and compare the performance of FinDer for four template sets (PGA w/o site corrections, and PGV w/o site corrections) generated with GMPEs after Bindi *et al.* (2011). **Figure 3.1.1** shows the spatially interpolated maps of near-source ground-motion amplitudes observed at RAN and RSN strong-motion stations during the three largest earthquakes of the 2016-2017 Central

Italy sequence: the Mw6.5 Norcia (top), the Mw6.0 Amatrice (middle), and the Mw5.9 Visso (bottom) earthquake. The maps show a clear elongation of the ground-motion amplitude pattern to the northwest.

For each of the three earthquakes and for each template set, we compute the best-fitting FinDer line-source model (black line with three yellow stars, **Figure 3.1.1**). We find that these models are in good agreement with the finite-fault models of Chiaraluce *et al.* (2017) and Tinti *et al.* (2016) with respect to their locations, lengths, and orientations (black rectangles, **Figure 3.1.1**). For reference, we also show the INGV point-source (epicentre) solutions (red stars, **Figure 3.1.1**).

Most strong-motions stations of the RSN and RAN networks are deployed on rock or stiff soil (class A and B, **Figure 1.1**), and the impact of site effects on ground-motion amplitudes is therefore likely to be less important in these events. This assumption is supported by our observation that the PGA and PGV ground-motion patterns in **Figure 3.1.1** are quite similar before and after the application of site corrections using correction factors according to Bindi *et al.* (2011). Tinti *et al.* (2016) argue that the distribution and variability of ground-motion amplitudes in the Mw6.0 Amatrice earthquake is mainly due to the effects of slip heterogeneity and rupture directivity. We suspect that this also applies to the Mw5.9 Visso and Mw6.5 Norcia earthquakes.

Regardless of the template set chosen, and thus regardless of the selected ground-motion metric, the resulting FinDer line-source models in **Figure 3.1.1** are similar in terms of length and orientation. The locations, however, are less robust and seem to be more affected by the choice of the intensity measure. Smaller differences in the results for PGA and PGV are expected, since these parameters are sensitive to the seismic radiation of high- and mid-frequency motions, respectively.

Figure 3.1.1 shows the *final* ground-motion distribution (similar to *ShakeMaps* by Wald *et al.* (1999)) and *final* FinDer line-source model. In real-time operation, FinDer will start reporting line-source models as soon as significant shaking initiates (e.g. once a threshold of 2 cm/s/s at two neighboured stations is exceeded). To mimic the temporal evolution of the FinDer line-source parameters, we plot in **Figures 3.1.2** to **3.1.4** the estimates of rupture length, magnitude, and rupture strike for all earthquakes in our dataset, each as a function of time from event origin.

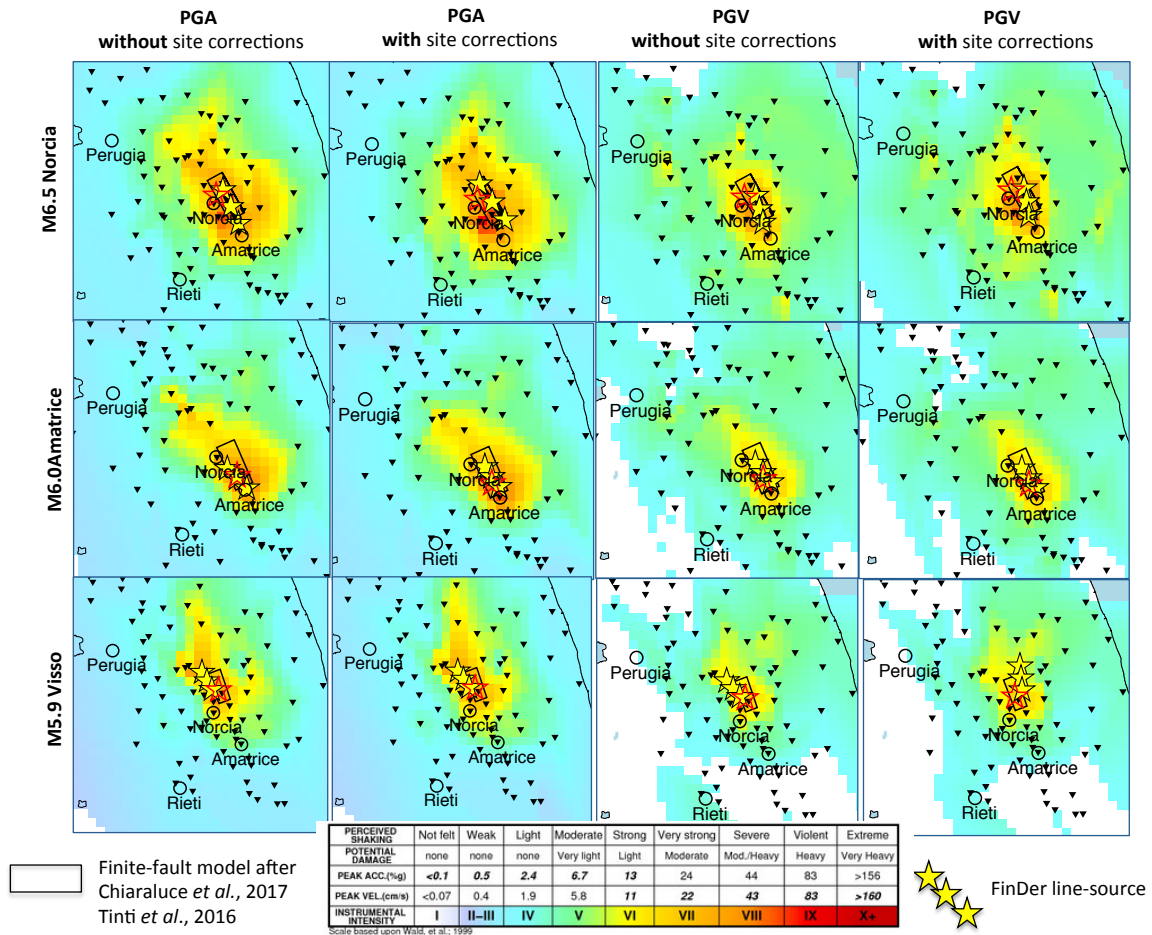


Figure 3.1.1. Spatial distribution of ground-motion amplitudes and FinDer determined line-source models in comparison with the finite-fault models of Tinti *et al.* (2016) and Chiaraluca *et al.* (2017). The models are in good agreement in terms of their locations, lengths, and orientations.

Assuming here a perfect system without any data latencies, the high density of strong-motion stations in the Central Apennines would allow us to detect all events in Central Italy within less than 5 seconds. For the largest events with $5.9 \geq M_w \geq 6.5$ we obtain stable line-source solutions within 10 to 15 seconds, and for the smaller events within less than 10 seconds. Although the line-source models tend to be better constrained in the larger Norcia, Amatrice, and Visso earthquakes, shown at the top of **Figures 3.1.2** to **3.1.4**, also for the smaller earthquakes the rupture strike tends to agree well with the $\sim 150^\circ$ strike of normal-fault system activated during the earthquake sequence (**Figure 1.1** and **Table 1.1**).

Would FinDer's line-source models have been useful for earthquake early warning (EEW) during the Central Italy sequence, if they had been determined in real-time? We plot in **Figure 3.1.5** the ground-motion prediction errors derived from the FinDer line-source models as a function of warning time. We define the prediction errors here as the logarithmic ratio of observed and predicted PGA amplitudes, the latter being predicted from GMPEs using the closest distance to the FinDer determined line-source at each time step. The warning time is defined as the time relative to the onset of weak (or stronger) shaking (Modified Mercally Intensity, $MMI \geq II$). In our analysis, we assess the errors for each recording station during the 13 test events in the sequence. Data latencies are again neglected.

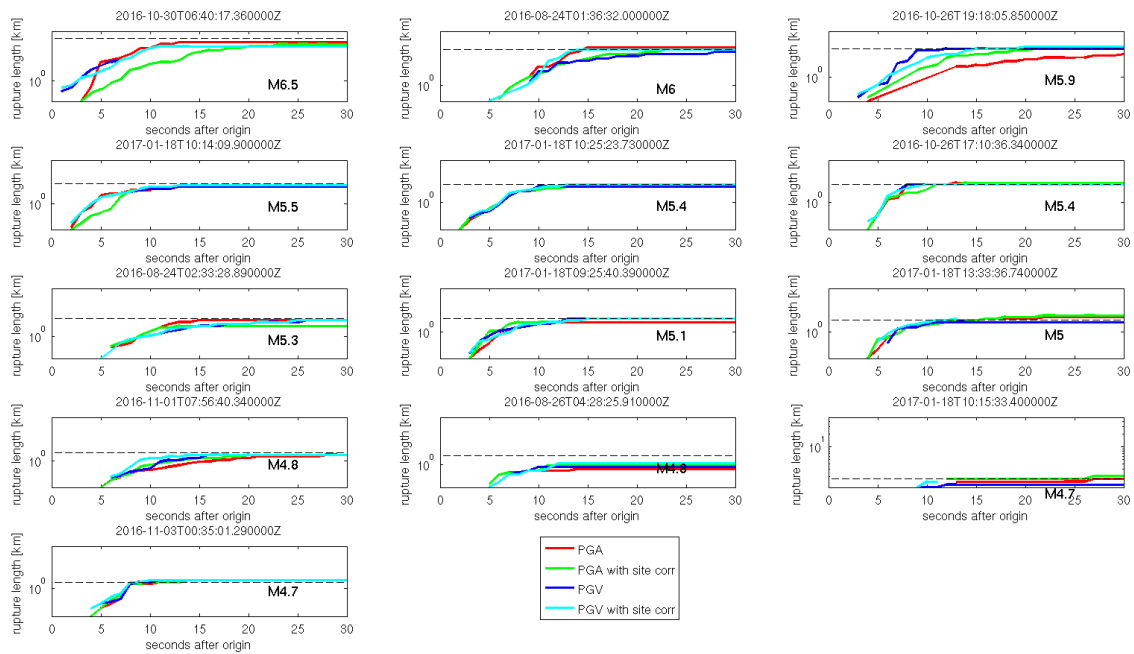


Figure 3.1.2. FinDer estimated rupture length as a function of time from event origin for each of the 13 events in the Central Italy sequence. Four template sets were used. Dashed lines show rupture length estimated from empirical magnitude-dependent relations following Wells and Coppersmith (1994).

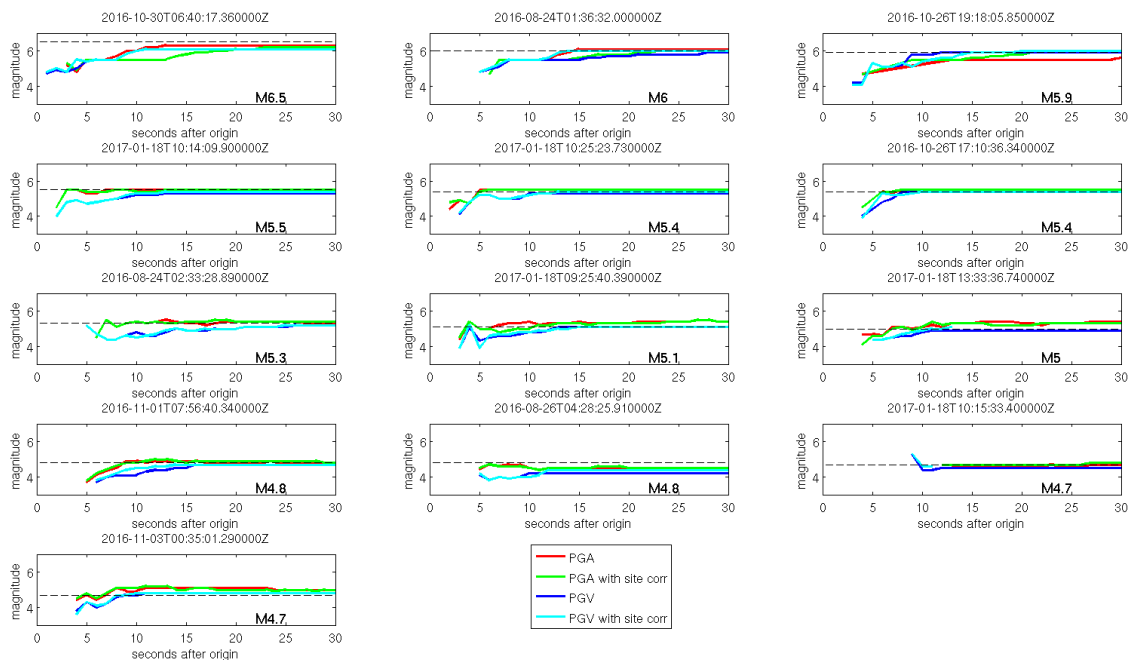


Figure 3.1.3. FinDer estimated magnitudes as a function of time from event origin, which are empirically derived from the length of the FinDer line-source models using relations by Wells and Coppersmith (1994).

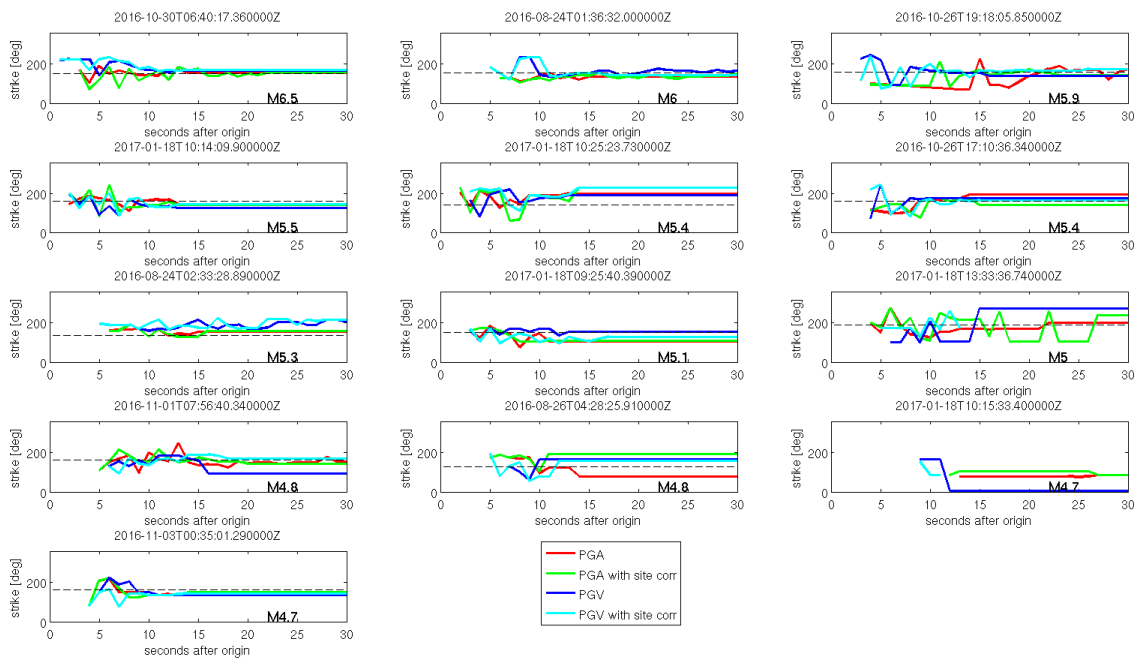


Figure 3.1.4. FinDer estimated rupture strike as a function of time from event origin. Note that for the M4.7 event on 2017-01-18, 10:15:33.4 no INGV focal mechanism and thus no strike estimate is available for comparison.

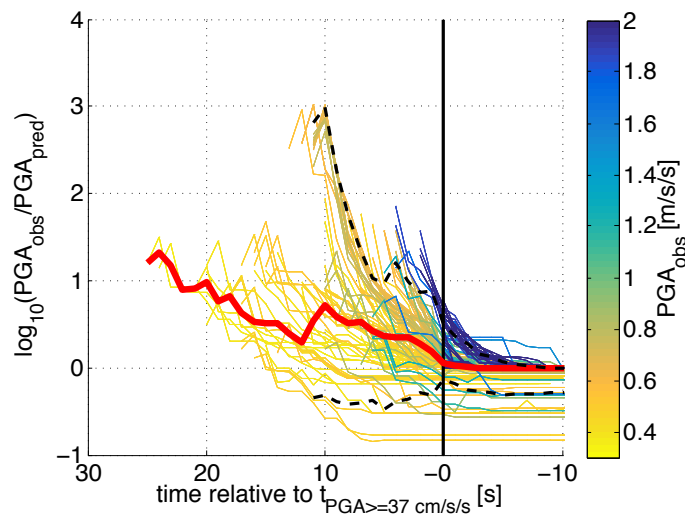


Figure 3.1.5. Ground-motion prediction errors as a function of warning time for all test events and all stations, neglecting data latencies. The prediction error is here defined as the logarithmic difference between the observed and predicted PGA (PGA_{obs} and PGA_{pred}). PGA_{pred} is predicted from GMPES according to Bindi *et al.* (2011) using the closest distance to the FinDer predicted line-source. Warning time is measured relative to the onset of weak shaking ($MMI=II$, $PGA=37\text{cm/s/s}$) at each recording station. Red line shows median prediction error, black dashed lines the 5th and 95th percentiles of error distributions. Warning times of more than 20 seconds are possible for a few sites with $MMI \geq II$, while most sites would get warning times of ≤ 10 seconds. Sites experiencing strongest shaking (dark blue) would only have a few seconds' warning time and would probably be in the EEW blind-zone if realistic delays were added.

Although some sites experiencing seismic intensities of $MMI \geq II$ (yellow lines, **Figure 3.1.5**) would have received a warning of more than 20 seconds before weak shaking at these sites initiates, the

majority of sites would have received a warning of about 10 seconds. Most shaken sites (dark blue lines, **Figure 3.1.5**) are usually near the earthquake epicentre, so would have received a few seconds of warning only. If realistic system delays were added, these sites are probably in the blind-zone of the warning system and would not have received a timely warning.

In addition to EEW, there are other benefits of providing finite-source information in (near) real-time, such as for rapid response following a destructive earthquake or for the calculation of aftershock probabilities. In **Figure 3.1.6 (top)** we plot the FinDer line-source models for the Mw6.5 Norcia, Mw6.0 Amatrice, and Mw5.9 Visso earthquakes at three time steps from event origin on top of INGV focal mechanisms, which were determined several hours after each event (**Table 1.1**). As time progresses, the FinDer models align more and more with the focal mechanisms and show a good agreement with the strike of the rupture planes in the INGV solutions. The same observation applies to a significant number of smaller earthquakes in the sequence (**Figure 3.1.6**, middle and bottom), though not all, because significant motion in the horizontal direction is required for FinDer to determine the orientation of the line-source. This observation is consistent with previous findings in California (Böse *et al.*, 2018), where we found that the strike of the FinDer line-source models usually coincides within 20° with one of the nodal planes of the focal mechanisms (usually, if determined, with the preferred plane) also for small and moderate-sized earthquakes and not just for strike-slip events.

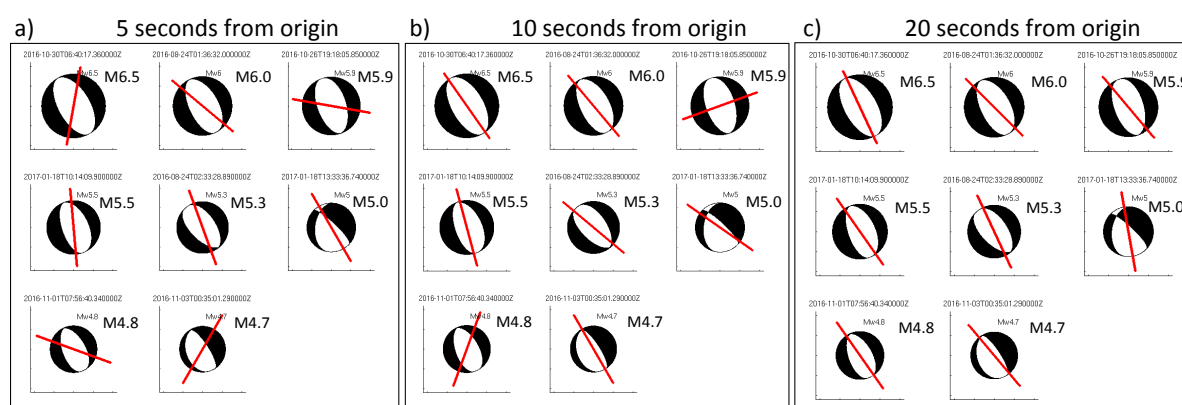


Figure 3.1.6. FinDer line-source models (red lines) on top of INGV focal mechanisms for the Mw6.5 Norcia, Mw6.0 Amatrice and Mw5.9 Visso earthquakes (top row), and five smaller events (middle and bottom) in the Central Italy sequence. As time progresses (from left to right), the FinDer models align more and more with the focal mechanisms and show a good agreement with the strike of the rupture planes in the INGV solutions.

This observation suggests an important role of rupture directivity in small earthquakes, causing asymmetric ground-motion patterns, and implies that the FinDer line-source models could help to quickly resolve fault-plane ambiguities for strike-slip events. This could then allow to quickly identify faults, along which rupture is occurring, and thus to provide more reliable estimates of aftershock probabilities compared to traditional, point-source approaches. Furthermore, the FinDer determined likelihood functions for rupture strike could be used as *prior* probabilities in initial focal mechanism solutions, as proposed in **Chapter 4**.

3.2 Rupture Dimensions, Moment Rate & Rapid Focal Mechanisms

Activity 1 – Real-Time Characterization of the Extended Seismic Source: For this activity, we expand our test dataset in **Table 1.1** and include a total of 28 earthquakes ($3.5 \leq Mw \leq 6.5$) of the 2016-2017 Central Italy earthquake sequence. We use a total of 1,895 strong motion waveforms recorded in epicentral distances of up to 100 km (**Figure 1.1**). These data were

selected to meet limiting signal-to-noise ratio criteria. For our analysis, we use only the vertical component of the ground motion records.

The observed and modelled curves in **Figure 3.2.1** show a consistent scaling with magnitude, both in the overall shape and in terms of scaling of P_L and T_L vs. magnitude M . Both the source radius and the half-duration parameter scale with magnitude, as is expected for a self-similar, constant stress-drop scaling ($\Delta\sigma = 2.1 \pm 4.4$ MPa). The largest earthquake of the sequence, the Mw6.5 Norcia earthquake, shows an apparent higher value of stress drop and shorter duration than expected from the scaling laws, which is consistent with other independent estimates of the same parameters (e.g. Picozzi *et al.*, 2017). Our proposed approach represents a fast, reliable alternative for a near real-time estimation of the source parameters (seismic moment, source radius, static stress drop). Results for the entire dataset are summarized in **Table 3.2.1**.

Table 3.2.1. Results of Activity 1 for the entire dataset.

Region event ID	Date time (UTC)	LAT [°]	LON [°]	Z [km]	ML	Mw	strike/dip/Rake [°]	Radius (km)	Half-Duration (s)	Release Time from O.T.(s)
A./AMatrice	24/08/16	42.6983	13.2335	8.1	6	6	155/49/-87	6.50	3.1	7.5
7073641	1:36:32 AM									
Norcia	24/08/16	42.7922	13.1507	8	5.4	5.3	135/47/-98	3.27	1.6	3.8
7076161	2:33:29 AM									
Amatrice	26/08/16	42.6048	13.2915	8.7	4.7	4.8	128/53/-106	3.45	1.6	3.9
7224451	4:28:26 AM									
C.S. Angelo	26/10/16	42.8802	13.1275	8.7	5.4	5.4	161/38/-90	4.32	2.1	5.0
8663031	5:10:36 PM									
Ussita/Visso	26/10/16	42.9087	13.1288	7.5	5.9	5.9	159/47/-93	7.17	3.5	8.3
8669321	7:18:06 PM									
Norcia	30/10/16	42.8322	13.1107	9.2	6.1	6.5	151/47/-89	5.04	2.4	5.8
8863681	6:40:17 AM									
Acquacanina	01/11/16	42.9902	13.1345	8.3	4.7	4.8	161/46/-82	4.52	2.2	5.2
9033461	7:56:40 AM									
Acquacanina	03/11/16	43.0277	13.0493	8.1	4.7	4.7	162/24/-76	1.90	0.9	2.2
9166761	12:35:01 AM									
Amatrice	18/01/17	42.545	13.2768	10	5.3	5.1	153/32/-88	3.58	1.7	4.2
12695491	9:25:40 AM									
Amatrice	18/01/17	42.531	13.2838	9.6	5.4	5.5	161/51/-86	4.99	2.4	5.8
12697591	10:14:10 AM									
Capitignano	18/01/17	42.5277	13.2852	8.8	4.7	-	unknown			
12697641	10:15:33 AM									
Amatrice	18/01/17	42.5033	13.277	9.4	5.3	5.4	140/35/-89	6.56	3.2	7.6
12698071	10:25:24 AM									
Monteale	18/01/17	42.4733	13.2747	9.5	5.1	5	188/30/-39	3.96	1.9	4.6
12707401	1:33:37 PM									

For each event, we also theoretically computed the time (from the event origin time) at which the information about seismic moment and source radius would be available. For the computation, we accounted for the delayed arrival of the P-wave measurements due to the source-to-receiver distance and assumed that the real-time evolution of LPDT curves reproduces the shape of the curves as observed in the off-line analysis. The time (in seconds from the origin time) at which the plateau of the curves would be available is also reported in **Table 3.2.1**.

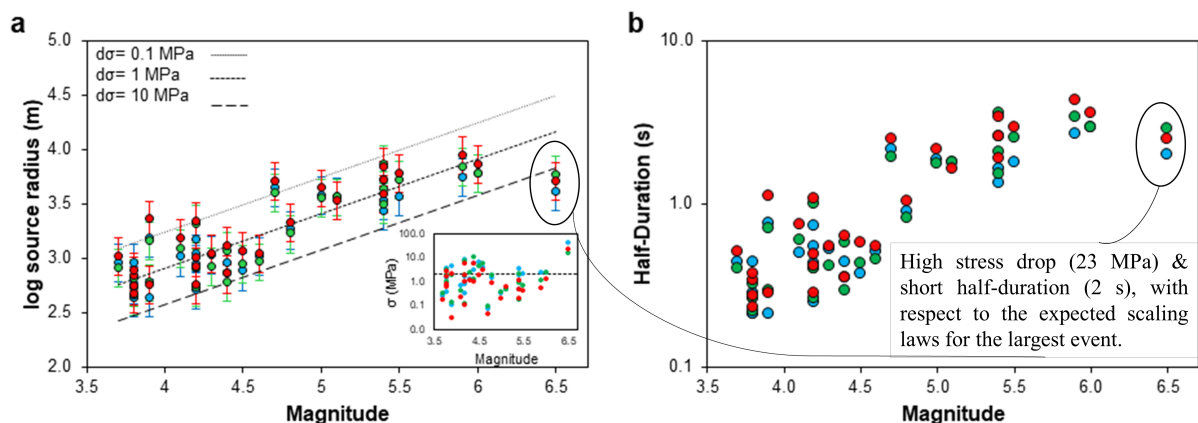


Figure 3.2.1. a) Scaling of the logarithm of the source radius with magnitude. The lines represent the theoretical scaling, with constant static stress-drop values (0.1, 1 and 10 MPa). The inset plot shows the estimated stress drop for the individual earthquakes in the selected dataset. The average stress drop value ($\Delta\sigma \cong 2.1$ MPa) is shown as a dashed line. (b) Half-duration of the source time function in terms of magnitude. In both panels, acceleration, velocity, and displacement data are shown with blue, green and red circles, respectively.

Activity 2 – Real-Time Fault-Plane Solution: We start our analysis for Activity 2 with the 2016 Mw6.5 Norcia earthquake, which is the strongest event of the 2016-2017 Central Italy sequence (**Table 1.1**). Focal mechanism solutions provided by national (INGV, **Table 1.1**) and international agencies (GFZ, USGS, GCMT) are quite different for this event, and vary between 151° and 162° in strike, between 27° and 47° in dip, and between -96° and -89° in slip (rake). Here we use a total of 67 (accelerometric) stations (**Figure 1.1**), with a maximum hypocentral distance of about 60 km. We simulate the real-time stream of data in order to account for the P-wave propagation arrival as a function of time.

Figure 3.2.2 shows the best solutions of strike, dip and slip at each iteration, starting from the P-wave arrival at the closest station. The inversion is performed in intervals of 1 s. For each step, the best solution (i.e., the most likely triplet of angles) and its uncertainty are shown. The uncertainties are computed as the 68% confidence ellipsoid's projections centred on the best solution. The algorithm starts reporting the outputs, when a pre-determined condition on the azimuthal coverage of stations is satisfied.

For the Mw 6.5 Norcia earthquake we use a total of 54 three-component accelerometric stations. The first solution is available about 4.7 s after the earthquake origin time, when data from 6 stations within 20 km of hypocentral distance are available, and the covering condition on the azimuthal distribution is satisfied. The convergence of the solution is reached after 4 iterations, i.e., 5 s after the arrival of first P-wave, which corresponds to 7.7 s after the origin time of the event (data latencies and computational times are not considered). At this time, the root mean square (rmsRMS) error of the solution reaches a stable value of 0.27. The final best solution (strike: $150^\circ \pm 8^\circ$; dip: $55^\circ \pm 4^\circ$; slip: $-94^\circ \pm 9^\circ$) includes the amplitude data from 30 stations within 35 km of hypocentral distance. The inferred solution presents relatively small errors (less than 10%) both on strike, dip and rake angles, and is consistent with the focal mechanism solution provided by the reference agency (INGV, see **Table 3.2.2**), with a K-angle of 9° . Results for the entire dataset are summarized in **Table 3.2.2**.

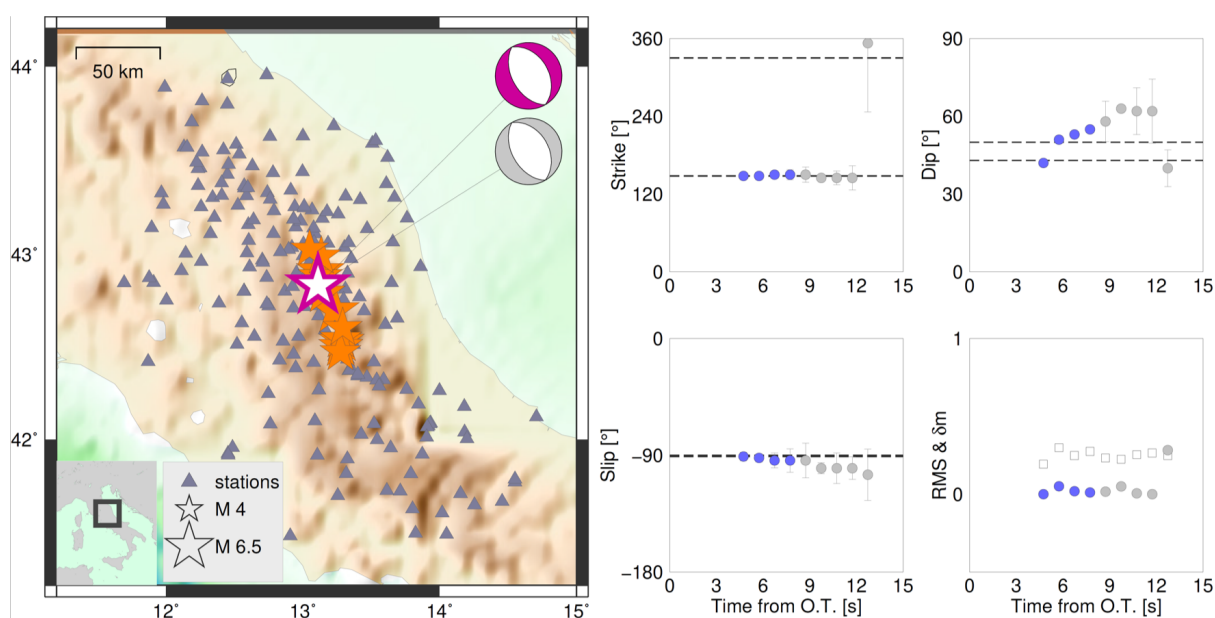


Figure 3.2.2. Results for the Mw 6.5 Norcia earthquake. The left-hand panel shows the epicentral location of

selected earthquakes of sequence (orange stars) and the recording stations (gray triangles). The size of the stars is proportional to the magnitude, and the main event is represented with a white star. The magenta beach-ball represents the INGV catalogue solution while the gray one shows our best solution. The right-hand panels show the solutions of strike, dip and slip at each iteration, starting from origin time. Blue dots represent the solutions up to the convergence, while grey dots represent the solution evolution after the convergence. Error bars show the 68% confidence ellipsoid projection on each solution. The bottom right panel shows the rms of each solution (empty squares) and the convergence condition (with blue and grey dots).

Table 3.2.2. Fault-plane solutions for the test dataset in **Table 1.1**.

Region, Event Id	INGV reference solution	MAP Model	median	Expected value	rms	Real time best solution	INGV reference solution
Accumoli, M_w 6.0 7073641	155/49/-87 331/41/-93	150/50/-105 355/38/-70	139/43/-117	150/50/-117	0.25		
Norcia, M_w 5.3 7076161	135/47/-98 327/43/-81	145/47/-100 339/44/-79	139/45/-83	139/45/-83	0.34		
Amatrice, M_w 4.8 7224451	128/53/-106 333/40/-70	149/45/-86 323/45/-94	148/43/-89	152/45/-89	0.34		
C.S. Angelo, M_w 5.4 8663031	161/38/-90 341/52/-90	173/35/-94 358/55/-87	150/38/-72	196/35/-72	0.17		
Ussita, M_w 5.9 8669321	159/47/-93 344/43/-87	162/36/-106 2/56/-79	185/36/-117	150/43/-117	0.29		
Norcia, M_w 6.5 8863681	151/47/-89 330/43/-91	150/55/-94 337/35/-84	139/55/-106	151/56/-106	0.27		
Acquacanina, M_w 4.8 9033461	161/46/-82 330/45/-98	150/43/-94 335/47/-86	139/45/-72	161/40/-72	0.33		
Acquacanina, M_w 4.7 9166761	162/24/-76 327/67/-96	162/28/-71 321/64/-100	164/35/-80	153/37/-80	0.32		
Amatrice, M_w 5.1 12695491	153/32/-88 331/58/-91	163/44/-76 324/48/-103	164/45/-78	160/43/-78	0.25		
Amatrice, M_w 5.5 12697591	161/51/-86 335/39/-95	151/66/-83 314/25/-105	151/58/-105	151/68/-105	0.16		
Capitignano 12697641							unknown
Amatrice, M_w 5.4 12698071	140/35/-89 319/55/-91	163/49/-80 328/42/-101	163/49/-80	165/46/-80	0.27		
Monte Reale, M_w 5.0 12707401	188/30/-39 313/71/-115	196/46/-50 326/57/-124	196/56/-71	184/60/-71	0.27		

3.3 Regional Moment Tensor & Rupture Directivity

In this study, we analyse the whole selected dataset of 13 normal faulting earthquakes from the 2016-2017 Central Italy seismic sequence, ranging in magnitude from M_w 4.7 to 6.5 (**Table 1.1**). We start our analysis simulating the detection of earthquakes, and assuming basic earthquake source information to be provided, including origin time, epicentral location and a first estimate of the magnitude. These parameters, according to the other early warning algorithms discussed in this report, are typically available within few tens of seconds from the earthquake origin time with sufficient accuracy.

For this analysis we use low frequency full waveforms recorded at broadband stations at local to regional distances. A latency time of 140 to 180 s is needed to ensure full waveforms recording at a sufficient number of stations in the region. This is because Central Italy presents a relatively high density of broadband seismic instruments, so that recordings at tens of stations with good azimuthal coverage is achieved within 2-3 minutes after the earthquake occurrence, but the latency time could be much larger at other locations. Data and metadata can be downloaded by the INGV web service in a few seconds and data are pre-processed to obtain downsampled (here 2 Hz) displacement traces rotated to radial, transversal and vertical components (here assuming the locations from the INGV catalogue in **Table 1.1**). The *prior* information on the magnitude is used to select the range of epicentral distances and frequency band to be used in the moment tensor and directivity inversion. For the selected dataset we use epicentral distances of 100-200, 125-225 and 150-250 km and bandpass

filters of 0.02-0.05, 0.017-0.04 and 0.01-0.04 Hz for events with magnitudes $M \leq 5.5$, $5.5 < M \leq 6.0$ and $M > 6.0$, respectively. Data selection has been performed here *a posteriori*, identifying and removing seismic stations, which iteratively reported data or metadata problems.

The moment tensor inversion is performed by fitting amplitude spectra of full waveforms for a pure DC and a full MT model, but we discuss here only DC sources. Centroid locations and mechanism polarity are resolved in a second step by fitting displacement waveforms in the time domain. Synthetic waveforms and spectra are computed using a pre-calculated Green's function database using the fomosto tool (Heimann *et al.*, 2016; Heimann *et al.*, 2017) and a regional crustal model for Central Italy from the CRUST2.0 database (Bassin *et al.*, 2000). Good quality moment tensor solutions are obtained for all events, with a good fit of waveform and spectra. The results reveal in all cases shallow (<12 km) centroid depths and NW-SE oriented normal faulting DC mechanisms. Moment magnitudes span from Mw 4.8 (Acquacarina) to 6.6 (Norcia), slightly larger than the original estimate in the INGV catalogue (**Table 1.1**). Source depths appear to be well resolved at least for moderate seismic events. Depth uncertainties are larger for larger events of $M > 6.0$, due to the fit of amplitude spectra and waveforms at lower frequencies; this explains the underestimation of the source depth for the M 6.6 Norcia earthquake.

The directivity analysis is performed at a later step, through the estimation of apparent durations at each station used, comparing full waveform amplitude spectra up to a frequency of 0.5 Hz. The azimuthal distribution of apparent duration can be fitted by different curves for pure unilateral and bilateral ruptures or by an average duration, if no clear directivity is resolved. Based on the F-test analysis (Cesca *et al.*, 2011), we identify 8 cases out of 13 with a clear dominant unilateral rupture direction (**Figure 3.3.1**).

In the majority of the cases the rupture direction is compatible with the fault strike, i.e. indicating a lateral directivity rather than a downdip or updip propagation. While we observe no predominant rupture direction throughout the whole dataset, directivity appears to be mostly toward SE during October-November 2016, and toward NW in January 2017. The derived source parameters for point source (best DC model) and finite source solutions are summarized in **Table 3.3.1**.

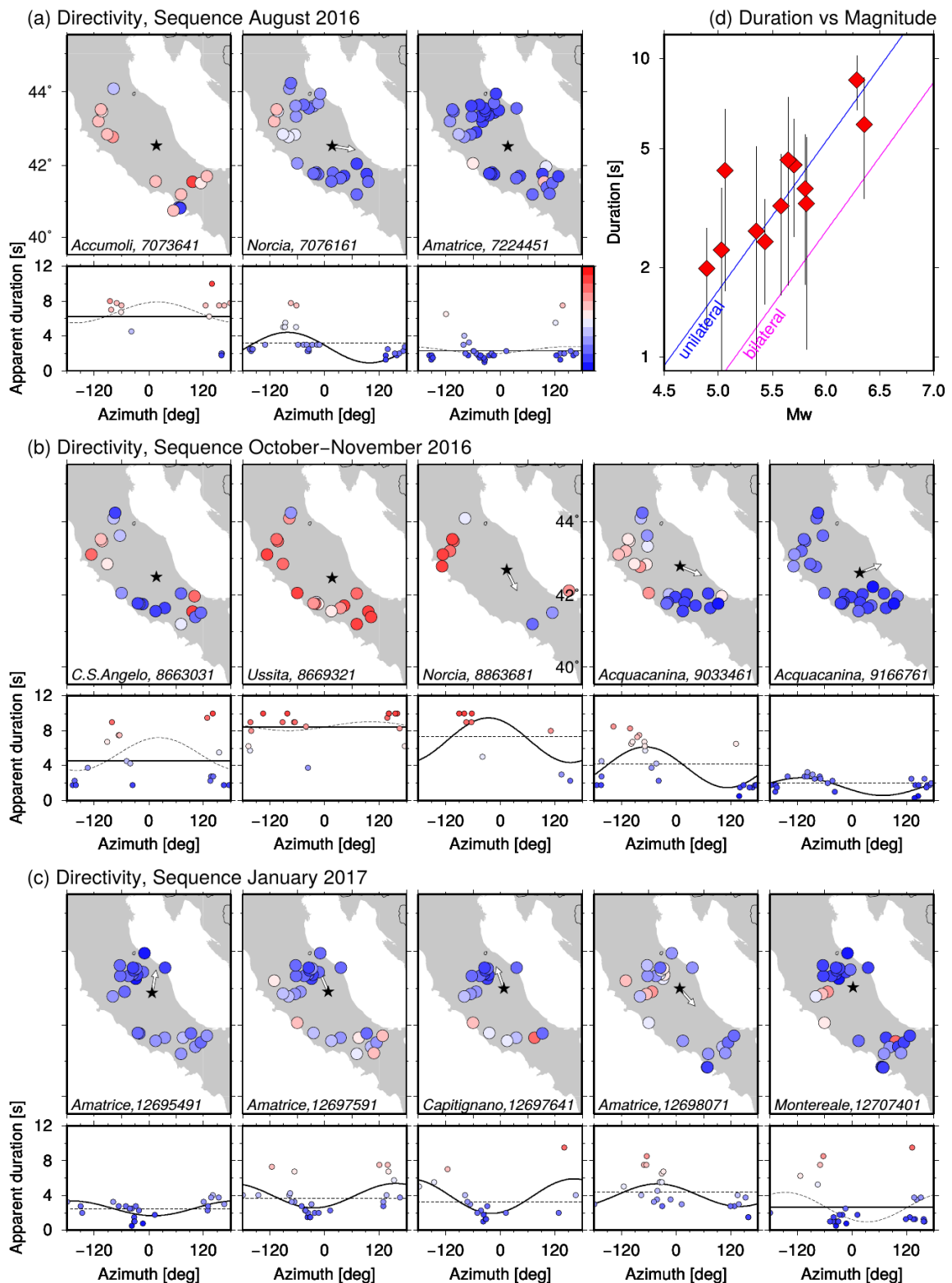


Figure 3.3.1. Apparent durations for all studied earthquakes (upper maps, circle colours representing durations according to the colour bar) and their azimuthal distribution (lower diagrams), modelled by a unilateral rupture (cosine curve) and an average duration (straight line); an F-test is used to define the preferred model (thick line) against the alternative model (thin dashed line). For unilateral rupture solutions, an arrow indicates the main rupture propagation direction. Plot (d) illustrates ranges of apparent durations (black bars) and average durations (red diamonds) as a function of moment magnitude (according to **Table 3.3.1**), together with durations for unilateral (blue line) and bilateral ruptures (pink line) based on empirical rupture lengths (Wells and Coppersmith, 1994).

Parameters directly resolved within the MT inversion are the strike, dip and rake for the two possible fault planes, the centroid depth, the scalar moment and consequently the moment magnitude. The magnitude is used to derive a first estimate of the rupture length, based on empirical relations (Wells and Coppersmith, 1994), which can be used to estimate a range of rupture durations assuming pure unilateral or bilateral rupture models and a fixed rupture velocity (here 2.5 km/s). The remaining parameters are directly obtained by the directivity inversion, through the analysis of apparent durations.

The fit of the azimuthal distribution of apparent duration is used to compute the average rupture duration and to detect directivity associated to dominant unilateral rupture and infer the main rupture direction. Finally, based on the rupture type and duration, and fixing P wave and rupture velocities, we obtain a second estimate of the rupture length. Different estimates of rupture lengths and durations, either based on empirical relations or inversion results, are in general agreement. Parameters directly resolved within the MT inversion are the strike, dip and rake for the two possible suggest slightly larger duration for the Central Italy sequence with respect to empirical values (**Figure 3.3.1d**), which can be due to a combination of dominant unilateral ruptures and slow rupture propagation at very shallow depth. The overall time required for the analysis, including latency, data download, pre-processing and inversion is about 3 to 4 minutes depending on the earthquake.

Table 3.3.1. Summary of source parameter results for the selected dataset.

REGION EVENT ID	STRIKE, DIP, RAKE [DEG]	DEPTH ⁽¹⁾ [KM]	M ₀ [NM], MW	DURATION ⁽²⁾ [S], LENGTH ⁽³⁾ [KM]	DIRECTIVITY ⁽⁴⁾ [TYPE, DEG]	DURATION ⁽⁵⁾ [S], LENGTH ⁽⁶⁾ [KM]
ACCUMOLI 7073641	153,62,-92; 336,28,-87	8.1	3.81e18; 6.4	4.0-7.9 s; 19.8 km	None	6.0 s; 15.0 km
NORCIA 7076161	141,62,-91; 324,28,-88	3.1	2.64e17; 5.6	1.6-3.3s; 8.1 km	Unilateral; 99° (ESE)	3.2s; 10.5 km
AMATRICE 7224451	136,55,-100; 332,36,-77	6.0	3.95e16; 5.0	0.9-1.7 s; 4.3 km	None	2.3 s; 5.7 km
C.S.ANGELO 8663031	172,67,-84; 338,23,-103	8.7	3.34e17; 5.6	1.8-3.5 s; 8.8 km	None	4.6 s; 11.4 km
USSITA 8669321	170,74,-83; 326,18,-113	7.5	3.02e18; 6.3	3.7-7.3 s; 18.3 km	None	8.5 s; 21.1 km
NORCIA 8863681	157,51,-88; 334,39,-92	1.2	8.89e18; 6.6	5.3-10.5 s; 26.3 km	Unilateral; 154° (SE)	7.4 s; 15.4 km
ACQUACANINA 9033461	152,67,-92; 338,23,-84	8.3	4.39e16; 5.0	0.9-1.8 s; 4.5 km	Unilateral; 113° (ESE)	4.2 s; 14.0 km
ACQUACANINA 9166761	158,29,-83; 330,61,-94	4.3	2.46e16; 4.8	0.7-1.5 s; 3.7 km	Unilateral; 68° (ENE)	2.0 s; 6.1 km
AMATRICE 12695491	145,29,-105; 342,62,-82	6.6	1.58e17; 5.4	1.4-2.7 s; 6.9 km	Unilateral; 10° (NNE)	2.4 s; 5.1 km
AMATRICE 12697591	157,56,-90; 336,34,-90	5.9	5.77e17; 5.8	2.1-4.2 s; 10.6 km	Unilateral; -23° (NNW)	3.7 s; 8.4 km
CAPITIGNANO 12697641	153,53,-95; 341,38,-83	8.8	5.96e17; 5.8	2.1-4.3 s; 10.7 km	Unilateral; -19° (NNW)	3.3 s; 11.9 km
AMATRICE 12698071	139,37,-94; 324,53,-87	7.2	4.02e17; 5.7	1.9-3.7 s; 9.4 km	Unilateral; 139° (SW)	4.4 s; 7.6 km
MONTEREALE 12707401	168,27,-72; 328,65,-99	11.6	1.21e17; 5.4	1.3-3.5 s; 6.3 km	None	2.6 s; 6.6 km

⁽¹⁾ Centroid depth from MT inversion; ⁽²⁾ Range of apparent durations estimated from the length⁽³⁾ assuming fixed rupture velocity (2.5 km/s) and as back-end cases pure unilateral and bilateral ruptures; ⁽³⁾ The length is estimated from the magnitude based on empirical relations (Wells and Coppersmith, 1994); ⁽⁴⁾ If a clear azimuthal pattern of apparent durations is detected, directivity is identified as unilateral, reporting the dominant rupture propagation direction, otherwise no directivity is reported; ⁽⁵⁾ Average apparent duration; ⁽⁶⁾

The length is inferred from average rupture duration and directivity, assuming a constant P wave and rupture velocity (6.0 km/s and 2.5 km/s).

3.4 Global Source Parameters

The fourth algorithm we test in this study, the Early-Est (EE) software, was designed to compute global source parameters for teleseismic earthquakes and thus requires that a minimum earthquake size to be exceeded ($M \sim 6.0$). Therefore, in this study we analyse the EE performance only for the three largest earthquakes in the 2016-2017 Central Italy sequence (2016 Mw6.0 Amatrice, Mw5.9 Visso, and Mw6.5 Norcia), but supplement this dataset by an additional 19 global earthquakes (**Table 1.2** and **Figure 1.2**) for a more systematic assessment. For evaluation we compare the source parameters computed by EE to those provided by the Global Centroid Moment Tensor (GCMT) for earthquakes that occurred after January 2017 and with the NEIC w-phase moment tensor solutions (mww) for the older events.

EE associates every minute all the earthquakes that have occurred during the previous hour. In this study, we analyse the EE solutions, which become available at 10 minutes from the origin time (OT) of each earthquake. This time window coincides approximately with either the solutions 005 or 008 used by the INGV-CAT (INGV Tsunami Alert Center) for issuing tsunami alerts (note that the alert provided by INGV-CAT should be provided by 14 minutes from OT). Nevertheless, the selection of this time window is somewhat arbitrary, since the time at which the first location estimates by EE become available depends on the location of the earthquake or - more specifically - on the source-receiver geometry of each individual earthquake. For example, locations and magnitudes for earthquakes in the Mediterranean area become available within 2 minutes, whereas it takes 5-6 minutes for earthquakes in other parts of the world with poorer station coverage.

3.4.1 Locations and Magnitudes

All EE locations analysed in this study were produced by the real-time system implemented at INGV and solutions were extracted from the INGV archive. These locations were obtained with a minimum of 29 and a maximum of 128 associated phases, depending on the different source-receiver geometries for different parts of the globe. In practice, EE adopts of the order of 450 seismic stations, which stream data to the real-time system. The number of available stations can vary by 10%-20% depending on the station availability.

In **Figure 3.4.1a**, we show the differences ($M_{GCMT} - M_{wp}$; $M_{GCMT} - M_{wpd}$) between the GCMT magnitudes and those obtained automatically using EE - M_{wp} and the M_{wpd} adopting a boxplot representation. These two magnitudes are determined automatically by EE without any expert/human revision. Both adopt only the P-pulse (M_{wp}) or the P-wave train as detected through the calculation of the high-frequency duration T_0 (M_{wpd}), and estimates are obtained very rapidly since they rely on P-waves. In detail, our results show that for the selected earthquakes M_{wp} has a small bias of 0.13 m.u. (std: 0.18) and a similar median value, implying that the M_{wp} solutions tend to underestimate the GCMT magnitude (for this relatively small data set). Conversely, almost no bias is observed for M_{wpd} (mean: 0.00; std: 0.15). In the INGV-CAT operational system, M_{wpd} supersedes M_{wp} for $M_{wp} \geq 7.2$ and, in general, it has been found to provide accurate estimates for large size earthquakes very rapidly (Lomax and Michelini, 2009; Bernardi *et al.*, 2015).

In **Figure 3.4.1b** (see also **Table 3.4.1**), we show the boxplot for epicentral distance and for depth. We note that for epicentral distance the minimum difference is less than 3 km (event_id: 20171031_004221.a), whereas values as large as 110-120 km are observed in two cases (event_id: 20171010_185341.a, 20170908_044946.a). In the first case (Bouvet Island Region), this large

difference in epicentral distance is likely caused by the almost simultaneous occurrence of 3 earthquakes, which likely reduced the quality of the stacking of the relatively small number of phases (34) used for the location. For the second case (M8.2 Near Coast of Chiapas, Mexico), the location difference is likely related to the large extension of the fault rupture (of the order of more than 100 km along strike) and the inherent difficulty to identify the earthquake focus uniquely.

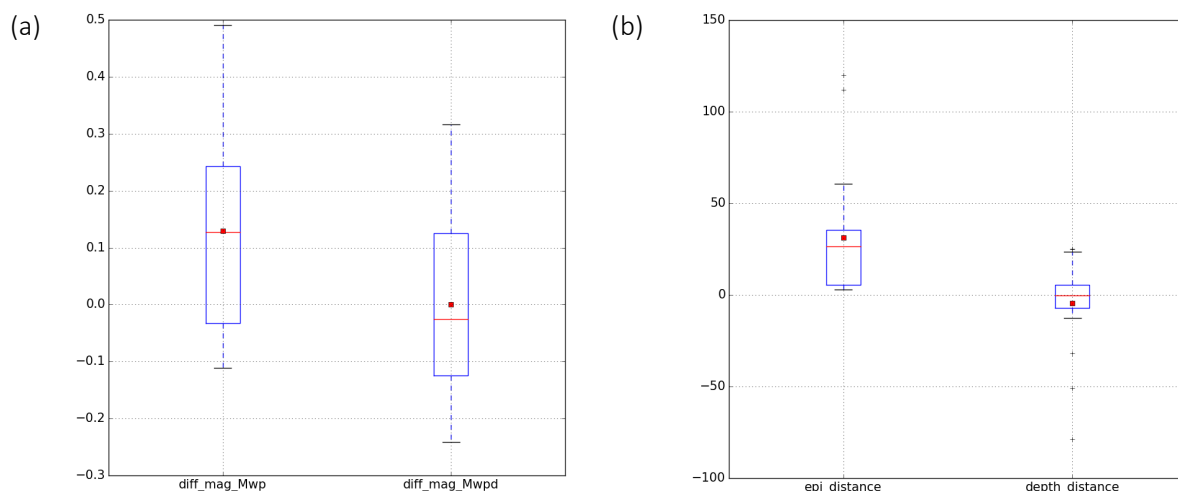


Figure 3.4.1. Boxplots showing the total extent of the 1st and 3rd quartile of the differences between (a) the GCMT and the Mwp (left) and Mwprd (right) estimates, and (b) the GCMT location for epicentral distance (left) and depth (right). The whiskers indicate the extent of the data. The red horizontal line pictures the median value and the red square the mean.

Table 3.4.1. Comparison of magnitudes and locations computed by the Early-Est software with the Global CMT solutions.

event_id	latitude	longitude	depth	M(GMT)	Mwp	Mwprd	epi dist.	depth dist	M - Mwp	M - Mwprd	#phases	std	n. evs	region
20180225_174508.a	-6.29	142.97	12	7.47	7.31	7.60	31.42	0.28	0.16	-0.13	72	1.19	4.00	New Guinea, Papua New Guinea
20180216_233946.a	16.53	-97.88	20	7.16	7.27	7.36	13.40	0.08	-0.11	-0.20	115	0.87	1.00	Oaxaca, Mexico
20180123_093204.a	56.22	-149.12	33.6	7.92	7.45	7.60	36.61	23.44	0.47	0.32	125	1.10	2.00	Gulf of Alaska
20180114_091852.a	-15.95	-74.78	40.9	7.12	6.99	7.15	31.97	25.28	0.13	-0.03	29	1.03	3.00	Near Coast of Peru
20180110_025144.a	17.56	-83.86	16.5	7.52	7.47	7.58	32.69	6.34	0.05	-0.06	33	1.14	1.00	North of Honduras
20171113_022829.a	9.45	-84.58	29.6	6.6	6.67	6.74	13.76	-5.17	-0.07	-0.14	120	1.25	1.00	Costa Rica
20171112_181825.a	34.83	45.84	17.9	7.4	7.14	7.30	2.83	8.13	0.26	0.10	107	0.89	3.00	Iran - Iraq Border Region
20171104_090031.a	-15.06	-173.09	35	6.71	6.68	6.76	29.19	24.84	0.03	-0.05	44	1.43	1.00	Tonga Islands
20171031_004221.a	-21.61	169.14	12.6	6.71	6.62	6.82	3.16	2.83	0.09	-0.11	54	1.28	3.00	Southeast of Loyalty Islands
20171024_104750.a	-7.25	123.02	556.8	6.72	6.44	6.56	5.99	-0.62	0.28	0.16	128	1.11	1.00	Banda Sea
20171010_185341.a	-53.89	8.92	16.4	6.73	6.35	6.64	120.08	-3.13	0.38	0.09	31	1.62	3.00	Bouvet Island Region
20170908_044946.a	15.38	-94.66	44.8	8.23	7.91	8.00	112.04	-12.62	0.32	0.24	122	1.10	1.00	Near Coast of Chiapas, Mexico
20170818_025939.a	-0.87	-14.15	22.2	6.63	6.45	6.59	56.96	-78.58	0.18	0.04	48	1.74	1.00	North of Ascension Island
20170720_223116.a	36.79	27.56	12	6.64	6.75	6.88	25.30	-7.73	-0.11	-0.24	96	1.06	1.00	Turkey
20170717_233457.a	54.13	169.78	23.2	7.76	7.27	7.61	60.68	13.04	0.49	0.15	72	1.23	1.00	Komandorskiye Ostrova Region
20170622_123109.a	13.57	-91.38	38.1	6.77	6.80	6.87	50.88	-31.82	-0.03	-0.10	119	1.02	1.00	Near Coast of Guatemala
20170614_072907.a	14.92	-92.17	72.7	6.95	6.79	6.81	27.30	-51.13	0.16	0.14	128	1.06	3.00	Guatemala
20170602_222454.a	54.14	170.83	13.1	6.74	6.62	6.69	2.84	2.94	0.12	0.05	75	1.53	1.00	Near Islands, Aleutian Islands
20170509_135215.a	-14.55	167.2	181.4	6.77	6.57	6.60	15.82	-8.44	0.20	0.17	65	1.23	1.00	Vanuatu Islands
20160824_013632.a	42.723	13.1877	4.44	6.2	6.23	6.22	3.83	-5.52	-0.03	-0.02	72	1.41	1.00	Central Italy
20161026_191808.a	42.9564	13.0666	10	6.1	6.15	6.24	5.17	-0.06	-0.05	-0.14	80	1.40	2.00	Central Italy
20161030_064018.a	42.8621	13.0961	8	6.6	6.66	6.82	4.56	-1.96	-0.06	-0.22	69	1.51	1.00	Central Italy

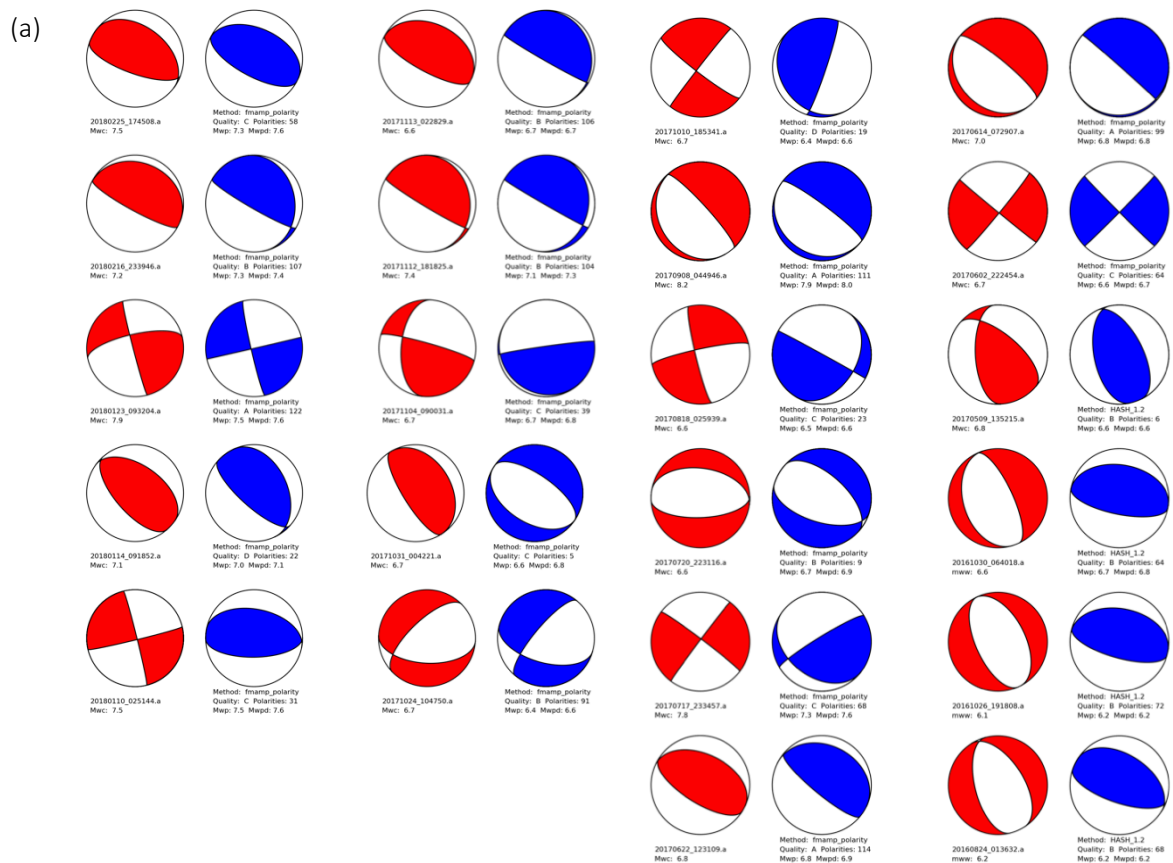
For depth, we observe that the differences are within a few kilometers with a median value close to zero. However, we also find a few notable outliers corresponding to the M6.6 North of Ascension Island (event_id: 20170818_025939.a) and two Guatemala events of M6.9 and M6.8, respectively (event_id: 20170614_072907.a, 20170622_123109.a). In the first case, the depth difference is to be attributed to a rather poor source-receiver geometry for locating earthquakes in that region (e.g., very few stations in Africa and S. America). For the same event (not shown here), the USGS-NEIC catalogue reports a depth of 35 km. For the two Guatemala events, the source of the difference is less clear given that in both cases the number of associated phases is quite large (128 and 119, respectively). We note, however, that the USGS-NEIC catalogue gives a depth of 93 km for the 20170614_072907.a event, which differs less significantly with the ~124 km depth resolved by EE at

10 minutes. These depth differences are expected to affect the determination of the fault-plane solutions, because they significantly change the take-off angles of the rays on the focal sphere.

3.4.2 Focal Mechanisms

The focal mechanisms for the analysed events are shown in **Figures 3.4.2**: the GCMT mechanisms were calculated from the moment tensor solutions; the EE mechanisms were determined using the newly developed software *fmamp_polarity* (starting 5/15/2017) and using the standard software HASH (Hardebeck and Shearer, 2008) for the earlier events (e.g., 2016 the Central Italy sequence), since the software *fmamp_polarity* software was not implemented at that time.

Examination of the EE solutions obtained at 10 minutes from OT shows that they are generally in agreement with those obtained from the formal inversion for the moment tensor of the GCMT. In general, we see that all the quality code “A” fault-plane solutions match closely those obtained from GCMT. The same, however, cannot be said for the other solutions that, although of lower quality “C” (or event “D”), they sometime match closely the GCMT solution closely. The 3 Central Italy sequence main events display a “B” quality evidencing that the mismatch owes primarily to the adoption of an incorrect velocity model.



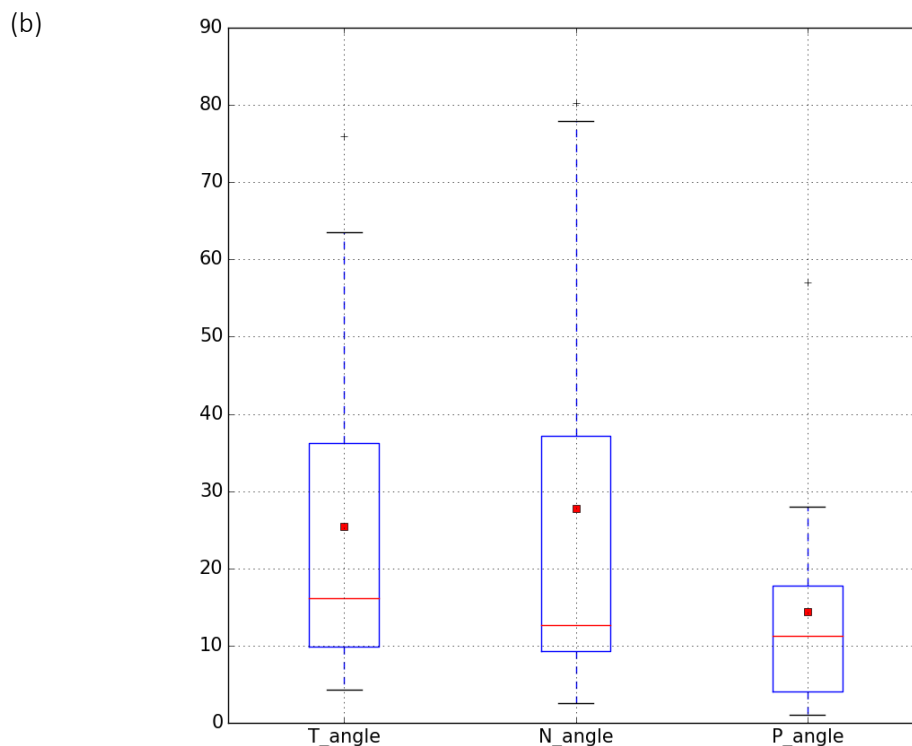


Figure 3.4.2. (a) Fault-plane solutions obtained using *fmamp_polarity* (blue) and from the GCMT moment tensor (red). For each solution we provide the event_id, the GCMT magnitude (M_{wc}), the method used by EE (i.e., *fmamp_polarity* or HASH), the quality of the solution (A-D, A best, D worst) and the M_{wp} and M_{wpd} magnitudes. (b) Boxplot summarizing the statistics for all 22 fault-plane solutions. The box indicates 50% of the data within the 2nd and 3rd quartile, the whiskers are drawn at nearly 3 standard deviation. The red horizontal line pictures the median value and the red square the mean.

In detail, in **Figure 3.4.2** we detect notable differences for the M7.5 North of Honduras event of January 10, 2018 (20180110_025144.a), which had fault-plane quality code “C” that misses the strike-slip mechanism resolved by the GCMT. Although there may be many factors influencing the calculation of the fault-plane solutions, we see that for this event only 30 polarities for the determination were used. Similarly, another notable difference is observed for the M6.7 October 31, 2017, in the Southeast of the Loyalty Islands. In this case, the quality code assigned by the *fmamp_polarity* software is “C”. Although the great majority of the EE fault-plane solutions fit nicely the mechanisms obtained through the GCMT, the three Central Italy main shocks (20160824_013632.a, 20161026_191808.a, 20161030_064018.a) provide a reverse fault mechanism opposite to the GCMT solution and the well-known dominant tectonic stress field there. Again, this discrepancy is likely caused by the peculiar velocity structure of the Apennines, which can strongly condition the take-off angles and the polarities used for the FP determinations.

3.4.3 Tsunami Discriminant

In **Figure 3.4.3**, we show the $TdT50Ex$ values plotted against the GCMT magnitude. We find that all the earthquakes with values of $TdT50Ex > 8.0$ (see LM2012 for detail), that have occurred at sea, were correctly identified as tsunamigenic. The only exception is the February 25, 2018, M7.5 Papua New Guinea earthquake (20180225_174508.a) with a value of 10, which is likely incorrect since in the same hour there have been recorded 3 other events and the $T0/T50Ex$ value is affected by the signal generated of the other earthquakes. Conversely, all the others with the exception of the Oaxaca, Mexico M7.2 onshore earthquake that occurred far from the coast, were identified correctly and are listed on the NOAA tsunami list (https://www.ngdc.noaa.gov/hazard/tsu_db.shtml).

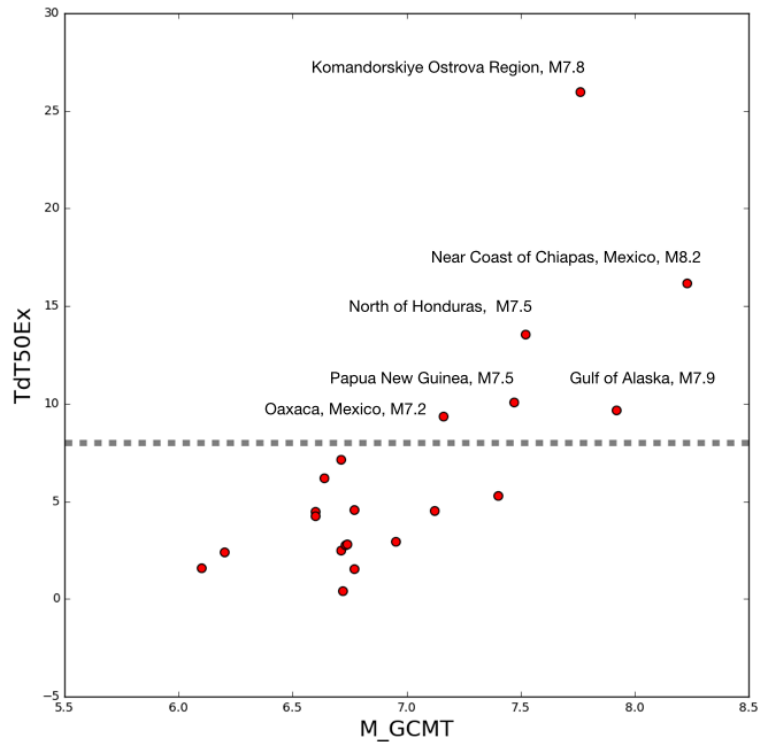


Figure 3.4.3. TdT50Ex discriminant plotted against magnitude (M_{GCMT}).

4 Conclusions

We use the example of the 13 largest events ($4.7 \leq M_w \leq 6.5$) in the 2016-2017 Central Italy earthquake sequence to demonstrate and compare in this study the performance of four independent algorithms developed at the four participating partner institutions in **WP 28, Task 1: Fault Geometry and Size**. For one of these algorithms (Early-Est), designed to characterize large earthquakes at teleseismic distances, we use an additional set of 19 global earthquakes ($6.6 \leq M_w \leq 8.2$) that occurred between 2017 and 2018.

The first algorithm, developed at **ETH Zurich**, provides quick event detections and line-source estimates for on-going earthquake ruptures based on template matching of high-frequency amplitudes (**Chapter 2.1**); the second set of algorithms, developed at **UNINA**, determines rupture dimensions, moment rate functions and rapid focal mechanisms from the temporal evolution and spatial distribution of peak amplitudes (**Chapter 2.2**); the third set of algorithms, developed at **GFZ Potsdam**, computes regional moment tensors by fitting the observed amplitude spectra and waveforms to those predicted by theoretical models; the analysis of apparent rupture duration allows to distinguish between uni- and bilateral fault ruptures (**Chapter 2.3**); and finally, the fourth algorithm, developed at **ALomax and INGV**, provides global source parameters, including event locations, magnitudes, fault-plane solutions, rupture durations and tsunami discriminants for offshore events (**Chapter 2.4**).

The first two algorithms derive source parameters from observed seismic near-source amplitudes, preferentially recorded at strong-motion/accelerometric stations to avoid amplitude clipping. If operated in a dense low-latency seismic network, both algorithms could provide preliminary finite-fault models within seconds from event origin, and hence could be useful for earthquake early warning (EEW). The other two algorithms are based on the inversion of regional and global broadband waveforms. If operated in an automated system, these algorithms could provide more

detailed finite-fault models within minutes from event origin, providing important information to rapid response for destructive earthquakes.

As demonstrated in this study, the first three algorithms provide robust finite-fault models of the 13 test events in Central Italy, which are consistent with the INGV earthquake catalogue (**Table 1.1**) and later determined finite-source solutions (e.g. Tinti *et al.*, 2016; Chiaraluce *et al.*, 2017; Scognamiglio *et al.*, 2018). In a simulated playback of waveforms recorded at the RAN and RSN strong-motion networks, the first algorithm detects all tests events within less than 5 seconds; stable line-source estimates (**Table 1.1**, top row) are obtained within 10 to 15 seconds for events with $M \geq 5.9$, and for smaller events within less than 10 seconds. For most events, in particular for the three largest events (Mw6.0 Amatrice, Mw5.9 Visso and Mw6.5 Norcia earthquakes), the line-source estimates agree well with the finite-fault models of Tinti *et al.* (2016) and Chiaraluce *et al.* (2017) and the overall strike of the normal-fault system in the Central Apennines. In this study, we tested template sets for different ground-motion metrics (PGA/PGV) w/o site corrections, and found that the resulting models are quite similar, indicating that the ground-motion patterns in the studied events are controlled largely by source complexities rather than site characteristics, which is consistent with earlier observations by Tinti *et al.* (2016).

The second set of algorithms estimates moment magnitudes, rupture dimensions and durations, as well as focal mechanisms from the temporal evolution and spatial distribution of near-source peak acceleration, velocity and displacement amplitudes. Aside from a few outliers (**Table 4.1**, second row from top), these results agree very well with the INGV catalogue and focal mechanisms (**Table 4.1**, bottom row) and could become available within 10 s, if data latencies are neglected.

Based on the inversion of amplitude spectra and waveforms from broadband stations at regional distances, these models are confirmed and refined by the third algorithm tested in this study. This algorithm provides moment tensors, rupture dimensions and durations, as well as the direction of lateral rupture propagation (uni- vs bilateral) from directivity analyses (**Table 4.1**, third row from top). Since sufficiently long waveform time-series must be available at regional distances, results from the third algorithms could become available within 2 minutes from event origin when operated in an automated system.

The fault-plane solutions obtained with the fourth algorithm (**Table 4.1**, second row from bottom) are incorrect (reverse rather than normal) for the three largest events in the Central Italy 2016-2017 sequence. This is likely caused by the complexity of the local velocity structure of the Apennines differing substantially from the global AK135 velocity model of Kennett *et al.* (1995), which is adopted for global earthquake location by Early-Est at the INGV-CAT TSP. Also the magnitudes are a bit overestimated compared to the INGV solution (**Table 1.1**) adopting a locally calibrated velocity model for the calculation of the Green's functions (unlike what is used in Early-Est in the global setup). For the second set of 19 global earthquakes ($6.6 \leq M_w \leq 8.2$), the algorithm, however, generally provides accurate results for location, earthquake size and tsunami discriminant within 10 minutes from event origin. We conclude that the Early-Est software, that is operational at the INGV-CAT, has confirmed its ability to provide accurate solutions, but suffers for some particular areas, such as Central Italy. In this study, we have chosen the 10 minutes after OT as target to verify the performance of the methodology, because it is well before the ~20 minutes time that is generally required to receive the first moment tensor solutions and it fits the requirements of INGV as NEAM Tsunami service provider.

Some of our algorithms employ empirical relationships, such as developed by Wells and Coppersmith (1994). Using alternative relations, such as proposed by Leonard (2014) for crustal ruptures or by Strasser *et al.* (2010) for subduction-zone earthquakes, might alter the algorithm performance for some earthquakes, which should be tested in future studies (in coordination with WP 25). Also systematic testing and comparison of different velocity models in various parts of Europe should be performed.

Table 4.1. Comparison of finite-fault models produced by the four algorithms (top to bottom) for the 13 test events (left to right). Largest events are highlighted in grey. Shown are the estimated line-sources (algorithm 1), and focal mechanisms (algorithms 2 to 4). Estimated parameters are the moment magnitude (M_w), source depth (Z), rupture length (L), rupture strike (Θ), and rupture duration (T). Grey arrows on top of focal mechanisms of algorithm 3 show rupture directivity. Catalogue parameters are shown in the bottom row. Further details on the events are given in **Table 1.1**. Algorithm 4, developed to process large teleseismic earthquakes, could only be tested for the largest three earthquakes. Fault-plane solutions of algorithm 4 are incorrect, likely caused by the complexity of the local velocity structure of the Apennines.

	Accum./Amatrice 7073641	Norcia 7076161	Amatrice 7224451	C. S. Angelo 8663031	Ussita/Visso 8669321	Norcia 8863681	Acquacania 9166761	Acquacania 9166761	Amatrice 12695491	Amatrice 122697591	Capitignano 12697641	Amatrice 12698071	Montereale 12707401
algorithm 1	 Mw6.1 L=15km $\Theta=135^\circ$	 Mw5.2 L=4km $\Theta=155^\circ$	 Mw4.5 L=1km $\Theta=89^\circ$	 Mw5.5 L=6km $\Theta=195^\circ$	 Mw5.9 L=11km $\Theta=150^\circ$	 Mw6.3 L=21km $\Theta=155^\circ$	 Mw4.7 L=2km $\Theta=155^\circ$	 Mw4.8 L=2km $\Theta=140^\circ$	 Mw5.3 L=2km $\Theta=105^\circ$	 Mw5.4 L=4km $\Theta=145^\circ$	 Mw4.7 L=2km $\Theta=85^\circ$	 Mw5.4 L=4km $\Theta=200^\circ$	 Mw5.2 L=4km $\Theta=200^\circ$
algorithm 2	 Mw6.0 L=13km T=6s	 Mw5.3 L=6-7km T=3s	 Mw4.8 L=7km T=3s	 Mw5.4 L=8-9km T=4s	 Mw5.9 L=14-15km T=7s	 Mw6.5 L=10km T=5s	 Mw4.8 L=9km T=4.5s	 Mw4.7 L=4km T=2s	 Mw5.1 L=7km T=3.5s	 Mw5.5 L=10km T=5s		 Mw5.4 L=13km T=6.5s	 Mw5.0 L=8km T=4s
algorithm 3	 Mw6.4, Z=8km L=15-20km T=6s uni (99°)	 Mw5.6, Z=3km L=8-11km T=3s uni (99°)	 Mw5.0, Z=6km L=4-6km T=2s	 Mw5.6, Z=9km L=9-11km T=5s	 Mw6.3, Z=8km L=18-21km T=7s uni (154°)	 Mw6.6, Z=1km L=15-26km T=7s uni (154°)	 Mw5.0, Z=8km L=5-14km T=4s uni (113°)	 Mw4.8, Z=4km L=4-6km T=2s uni (68°)	 Mw5.4, Z=7km L=5-7km T=2s uni (10°)	 Mw5.8, Z=6km L=8-11km T=4s uni (-23°)	 Mw5.8, Z=9km L=11-12km T=3s uni (-19°)	 Mw5.7, Z=7km L=8-9km T=4s uni (139°)	 Mw5.4, Z=12km L=6-7km T=3s
algorithm 4	 Mw6.2, Z=10km T=6s				 Mw6.2, Z=10km T=6s	 Mw6.7, Z=10km T=10s							
catalog	 Mw6.0, Z=8km L=13km	 Mw5.3, Z=8km L=4km	 Mw4.8, Z=9km L=2km	 Mw5.4, Z=9km L=5km	 Mw5.9, Z=8km L=11km	 Mw6.5, Z=9km L=29km	 Mw4.8, Z=8km L=2km	 Mw4.7, Z=8km L=2km	 Mw5.1, Z=10km L=3km	 Mw5.5, Z=10km L=6km	 Mw4.7, Z=9km L=2km	 Mw5.4, Z=9km L=5km	 Mw5.0, Z=10km L=3km

Together, the four algorithms provide a continuous spectrum of earthquake information, covering various aspects of on the fault geometry and size, and as such could provide crucial information in the case of destructive earthquakes in Europe and around the globe if operated in automated systems. In future studies, we plan to investigate in more detail, how the various algorithms could benefit each other by exchanging information that could for example be used as *prior* information in other methods. Obvious candidates are the strike likelihood function of the line-source model determined in the first algorithm (**Chapter 2.1**), and the focal mechanism determined by the second method (**Chapter 2.2**). Another example is the catalogue information required in the moment tensor inversion in the third algorithm (**Chapter 2.3**) that could be provided by the first two algorithms. Other information (e.g. the focal mechanisms and moment tensors provided by algorithms 2, 3 and 4) might be redundant and as such might help to confirm or reject earlier finite-fault models.

5 References

- Aki, K. and P. G. Richards (1980). *Quantitative Seismology: Theory and Methods*, W. H. Freeman and Company.
- Bassin, C., Laske, G., and G. Masters (2000). The current limits of resolution for surface-wave tomography in North America. *Eos. Trans. AGU* 81, F897.
- Bernardi, F., A. Lomax, A. Michelini, V. Lauciani, A. Piatanesi, and S. Lorito (2015). Appraising the Earliest earthquake monitoring system for tsunami alerting at the Italian Candidate Tsunami Service Provider, *Nat. Hazards Earth Syst. Sci.*, 15(9), 2019–2036, doi:10.5194/nhess-15-2019-2015.
- Bindi, D., F. Pacor, L. Luzi, R. Puglia, M. Massa, G. Ameri, and R. Paolucci (2011). Ground motion prediction equations derived from the Italian strong motion database, *Bull. Earthq. Eng.* 9, 1899–1920.
- Böse, M., T.H. Heaton, and E. Hauksson (2012). Real-time Finite Fault Rupture Detector (FinDer) for Large Earthquakes, *Geophys. J. Int.* 191(2), 803–812, doi:10.1111/j.1365-246X.2012.05657.x.
- Böse, M., C. Felizardo, and T.H. Heaton (2015). Finite-Fault Rupture Detector (FinDer): Going Real-Time in Californian ShakeAlert Warning System, *Seismol. Res. Lett.* 86(6), 1692–1704, doi:10.1785/0220150154.
- Böse, M., D.E. Smith, C. Felizardo, M.-A. Meier, T.H. Heaton, and J.F. Clinton (2018). FinDer v.2: Improved real-time ground-motion predictions for M2–M9 with seismic finite-source characterization, *Geophys. J. Int.* 212(1), 725–742, doi: 10.1093/gji/ggx430.
- Cesca, S., S. Heimann, K. Stammer, and T. Dahm (2010). Automated point and kinematic source inversion at regional distances, 2010. *J. Geophys. Res.*, 115, B06304, doi:10.1029/2009JB006450.
- Cesca, S., S. Heimann, and T. Dahm (2011). Rapid directivity detection by azimuthal amplitude spectra inversion. *J. Seismol.*, 15, 1, 147–164, doi: 10.1007/s10950-010-9217-4.
- Cesca, S., T. Dahm, C. Juretzek and D. Kühn (2011). Rupture process of the 7 May 2001 Mw 4.3 Ekofisk induced earthquake, *Geophys. J. Int.*, doi: 10.1111/j.1365-246X.2011.05151.x.
- Cesca S., T. Braun, F. Maccaferri, L. Passarelli, E. Rivalta, and T. Dahm (2013). Source modelling of the M5-6 Emilia-Romagna, Italy, earthquakes (May 20-29, 2012). *Geophys. J. Int.*, doi: 10.1093/gji/ggt069.
- Cesca, S., Grigoli, F., Heimann, S., Gonzalez, A., Buforn, E., Maghsoudi, S., Blanch, E., and T. Dahm (2014). The 2013 September-October seismic sequence offshore Spain: a case of seismicity triggered by gas injection? *Geophys. J. Int.*, 198, 2, 941–953.
- Cesca, S., Grigoli F., Heimann F., Dahm T., Kriegerowski, M., Sobiesiak M., Tassara C., and Olcay M. (2016). The Mw 8.1 2014 Iquique, Chile, seismic sequence: a tale of foreshocks and aftershocks, *Geophys. J. Int.*, doi: 10.1093/gji/ggv544.
- Cesca, S., Heimann, S., Kriegerowski, M., Saul, J., and Dahm, T. (2017). Seismic analysis of nuclear explosions: what can we learn from the January 6 and September 2016 nuclear tests, North Korea? *Seismol. Res. Lett.*, doi: 10.1785/0220160139.
- Chiaraluce, L., R. Di Stefano, E. Tinti, L. Scognamiglio, M. Michele, E. Casarotti, M. Cattaneo, P. De Gori, C. Chiarabba, G. Monachesi, A. Lombardi, L. Valoroso, D. Latorre, S. Marzorati (2017). The 2016 Central Italy Seismic Sequence: A First Look at the Mainshocks, Aftershocks, and Source Models, *Seismol. Soc. Am.* 88(3), doi: 10.1785/0220160221.
- Colombelli, S., and A. Zollo (2015), Fast determination of earthquake magnitude and fault extent from real-time P-wave recordings, *Geophys. J. Int.*, 502, 1158–1163, doi: 10.1093/gji/ggv217.

- Custodio, S., S. Cesca, and S. Heimann (2012). Fast kinematic waveform inversion and robustness analysis: Application to the 2007 Mw5.9 Horseshoe Abyssal Plain, offshore SW Iberia, Earthquake, *Bull. Seismol. Soc. Am.*, 102, 361-376.
- Del Fresno, C., Domínguez Cerdeña, I., Cesca, S., and E. Buforn (2015). The 8 October 2011 Earthquake at El Hierro (Mw 4.0): Focal Mechanism of the Main Shock and Its Foreshocks, *Bull. Seismol. Soc. Am.*, 105, 1, doi: 10.1785/0120140151.
- Domingues A., S. Custodio, and S. Cesca (2013). Waveform Inversion of Small to Moderate Earthquakes Located Offshore Southwest Iberia, *Geophys. J. Int.*, doi: 10.1093/gji/ggs010.
- Dziewonski, A. M., T.-A. Chou and J. H. Woodhouse, Determination of earthquake source parameters from waveform data for studies of global and regional seismicity, *J. Geophys. Res.*, 86, 2825-2852, 1981. doi:10.1029/JB086iB04p02825
- Ekström, G., M. Nettles, and A. M. Dziewonski, The global CMT project 2004-2010: Centroid-moment tensors for 13,017 earthquakes, *Phys. Earth Planet. Inter.*, 200-201, 1-9, 2012. doi:10.1016/j.pepi.2012.04.002
- Fang, S., Huang, S., Srinivasan, R., Raghavan, R., 1996. Deformable volume rendering by 3D texture mapping and octree encoding. IEEE Computer Society Press Los Alamitos, CA, USA. ISBN:0-89791-864-9.
- Grigoli, F., S. Cesca, A. P. Rinaldi, A. Manconi, J. A. Lopez Comino, J. Clinton, R. Westaway, C. Cauzzi, T. Dahm, and S. Wiemer (2018). The November 2017 Mw 5.5 Pohang earthquake: A possible case of induced seismicity in South Korea, *Science*, doi: 10.1126/science.aat2010
- Hardebeck, J. L. and Shearer, P. M. (2002). A new method for determining firstmotion focal mechanisms. *Bull. Seismol. Soc. Am.*, 92:2264-2276.
- Hardebeck, J. L. and Shearer, P. M. (2003). Using S/P Amplitude Ratios to Constrain the Focal Mechanisms of Small Earthquakes. *Bull. Seismol. Soc. Am.*, 93:2434-2444.
- Hardebeck, J. L., and P. M. Shearer (2008), HASH: A FORTRAN Program for Computing Earthquake First-Motion Focal Mechanisms–v1. 2–January 31, 2008,
- Heimann, S., Kriegerowski, M., Dahm, T., Cesca, S., and R. Wang (2016). A Green's function database platform for seismological research and education: applications and examples. EGU General Assembly 2016, Vienna, Austria.
- Heimann, S., Kriegerowski, M., Isken, M., Cesca, S., Daout, S., Grigoli, F., Juretzek, C., Megies, T., Nooshiri, N., Steinberg, A., Sudhaus, H., Vasyura-Bathke, H., Willey, T., and T. Dahm (2017). Pyrocko - An open-source seismology toolbox and library. V. 0.3. GFZ Data Services. doi: doi.org/10.5880/GFZ.2.1.2017.001.
- Kanamori, H., 2005. Real-time seismology and earthquake damage mitigation, *Annu. Rev. Earth Planet. Sci.*, 33, 195–214, doi:10.1146/annurev.earth.33.092203.122626.
- Keilis-Borok, V.I., 1959. On estimation of the displacement in an earthquake source and of source dimensions, *Ann. Geofis.*, 12, 205–214.
- Kennett, B. L. N., E. R. Engdahl, and R. Buland (1995). Constraints on seismic velocities in the Earth from traveltimes. *Geophysical Journal International* **122**, 108–124.
- Lavecchia, G., Brozzetti, F., Barchi, M., Menichetti, M. and Keller, J.V., 1994. Seismotectonic zoning in east-central Italy deduced from an analysis of the Neogene to present deformations and related stress fields. *Geol. Soc. Am. Bull.*, 106 1107-1120.

- Leonard, M. (2014). Self-Consistent Earthquake Fault-Scaling Relations: Up-date and Extension to Stable Continental Strike-Slip Faults, *Bull. Seism. Soc. Am.* 104, 2953–2965, doi: 10.1785/0120140087.
- Lomax, A., and A. Michelini (2009), M wpd: a duration-amplitude procedure for rapid determination of earthquake magnitude and tsunamigenic potential from Pwaveforms, *Geophys. J. Int.*, 176(1), 200–214, doi:10.1111/j.1365-246X.2008.03974.x.
- Lomax, A. J., and A. Michelini (2012). Tsunami Early Warning Within Five Minutes, *Pure Appl. Geophys.*, 1–11, doi:DOI 10.1007/s00024-012-0512-6.
- Lomax, A., A. Michelini, A. Curtis (2009). Earthquake Location, Direct, Global-Search Methods, in Encyclopedia of Complexity and System Science, Part 5, Meyers, R. A. (ed.), Springer, New York, pp. 2449-2473, doi:10.1007/978-0-387-30440-3.
- Luzi, L., R. Puglia, E. Russo, M. D'Amico, C. Felicetta, F. Pacor, G. Lanzano, U. Çeken, J. Clinton, G. Costa, L. Duni, E. Farzanegan, P. Gueguen, C. Ionescu, I. Kalogeras, H. Özener, D. Pesaresi, R. Sleeman, A. Strollo, and M. Zare (2016). The Engineering Strong-Motion Database: A Platform to Access Pan-European Accelerometric Data, *Seismol. Res. Lett.* 87(4), doi: 10.1785/0220150278.
- Picozzi, M., D. Bindi, P. Brondi, D. Di Giacomo, S. Parolai, and A. Zollo (2017), Rapid determination of Pwave-based energy magnitude: Insights on source parameter scaling of the 2016 Central Italy earthquake sequence, *Geophys. Res. Lett.*, 44, 4036–4045, doi:10.1002/2017GL073228.
- Reasenber, P. and Oppenheimer, D. (1985). Pffit, fplot, and fppage: Fortran computer programs for calculating and displaying earthquake fault plane solutions. Technical report, U.S. Geol. Survey.
- Scognamiglio, L., E. Tinti, E. Casarotti, S. Pucci, F. Villani, M. Cocco, F. Magnoni, A. Michelini, and D. Dreger (2018). Complex Fault Geometry and Rupture Dynamics of the M W6.5, 30 October 2016, Central Italy Earthquake, *Journal of Geophysical Research-Solid Earth*, 53(2), 557–22, doi:10.1002/2018JB015603.
- Spudich, P., and B.S.J. Chiou (2008). Directivity in NGA Earthquake Ground Motions: Analysis Using Isochrone Theory, *Earthquake Spectra* 24(1), 279-298, doi: http://dx.doi.org/10.1193/1.2928225.
- Strasser, F.O., Arango, M.C., Bommer, and J.J. (2010). Scaling of the Source Dimensions of Interface and Intraslab Subduction-zone Earthquakes with Moment Magnitude. *Seismological Research Letters*, 81(6), 941-950.
- Stucchi, M., et al. (2011), Seismic hazard assessment (2003–2009) for the Italian building code, *Bull. Seismol. Soc. Am.* 101(4), 1885–1911, doi:10.1785/0120100130.
- Tinti, E., L. Scognamiglio, A. Michelini, and M. Cocco (2016). Slip heterogeneity and directivity of the M_L 6.0, 2016, Amatrice earthquake estimated with rapid finite-fault inversion, *Geophys. Res. Lett.* 43,745-752, doi:10.1002/2016GL071263.
- Wald, D.J., V. Quitoriano, T.H. Heaton, H. Kanamori, C.W. Scrivner, and C. B. Worden (1999). TriNet “ShakeMaps”: Rapid Generation of Peak Ground Motion and Intensity Maps for Earthquakes in Southern California, *Earthquake Spectra* 15(3), 537-555.
- Wells, D. L., and K. J. Coppersmith (1994). New Empirical Relationships among Magnitude, Rupture Length, Rupture Width, Rupture Area, and Surface Displacement, *Bull. Seismol. Soc. Am.*, 84, 4, 974-1002.

Contact

Project lead	ETH Zürich
Project coordinator	Prof. Dr. Domenico Giardini
Project manager	Dr. Kauzar Saleh
Project office	ETH Department of Earth Sciences Sonneggstrasse 5, NO H62, CH-8092 Zürich sera_office@erdw.ethz.ch +41 44 632 9690
Project website	www.sera-eu.org

Liability claim

The European Commission is not responsible for any use that may be made of the information contained in this document. Also, responsibility for the information and views expressed in this document lies entirely with the author(s).